Johannes Rembe | Edward R. Sobel | Jonas Kley | Baiansulu Terbishalieva | Antje Musiol | Jie Chen | Renjie Zhou

Geochronology, Geochemistry, and Geodynamic Implications of Permo-Triassic Back-Arc Basin Successions in the North Pamir, Central Asia

Suggested citation referring to the original publication:
Lithosphere (2022), pp. 1 - 21
DOI https://doi.org/10.2113/2022/7514691
ISSN 1947-4253

Journal article | Version of record

Secondary publication archived on the Publication Server of the University of Potsdam:
Zweitveröffentlichungen der Universität Potsdam :
Mathematisch-Naturwissenschaftliche Reihe 1309
ISSN: 1866-8372
https://nbn-resolving.org/urn:nbn:de:kobv:517-opus4-583318
DOI: https://doi.org/10.25932/publishup-58331

GeoScienceWorld
Lithosphere
Volume 2022, Article ID 7514691, 21 pages
https://doi.org/10.2113/2022/7514691

Lithosphere

Research Article

Geochronology, Geochemistry, and Geodynamic Implications of Permo-Triassic Back-Arc Basin Successions in the North Pamir, Central Asia

Johannes Rembe[1], **Edward R. Sobel**[1], **Jonas Kley**[2], **Baiansulu Terbishalieva**[3], **Antje Musiol**[1], **Jie Chen**[4] and **Renjie Zhou**[5]

[1]*Institute of Geosciences, University of Potsdam, 14476 Potsdam, Germany*
[2]*Department of Structural Geology and Geodynamics, Georg-August-Universität Göttingen, 37077 Göttingen, Germany*
[3]*Institute of Geology, National Academy of Sciences of the Kyrgyz Republic, Laboratory of Metamorphic Formations, Erkindik Avenue-30, Bishkek 720481, Kyrgyzstan*
[4]*State Key Laboratory of Earthquake Dynamics, Xinjiang Pamir Intracontinental Subduction National Field Observation and Research Station, Institute of Geology, China Earthquake Administration, Chaoyang, 100029 Beijing, China*
[5]*School of Earth and Environmental Sciences, The University of Queensland, St. Lucia QLD 4072, Australia*

Correspondence should be addressed to Johannes Rembe; jrembe@uni-potsdam.de

Received 5 May 2022; Revised 1 September 2022; Accepted 29 September 2022; Published 6 December 2022

Academic Editor: Pierre Valla

The Permo-Triassic period marks the time interval between Hercynian (Variscan) orogenic events in the Tien Shan and the North Pamir, and the Cimmerian accretion of the Gondwana-derived Central and South Pamir to the southern margin of the Paleo-Asian continent. A well-preserved Permo-Triassic volcano-sedimentary sequence from the Chinese North Pamir yields important information on the geodynamic evolution of Asia's pre-Cimmerian southern margin. The oldest volcanic rocks from that section are dated to the late Guadalupian epoch by a rhyolite and a dacitic dike that gave zircon U-Pb ages of ~260 Ma. Permian volcanism was largely pyroclastic and mafic to intermediate. Upsection, a massive ignimbritic crystal tuff in the Chinese Qimgan valley was dated to 244.1 ± 1.1 Ma, a similar unit in the nearby Gez valley to 245 ± 11 Ma, and an associated rhyolite to 233.4 ± 1.1 Ma. Deposition of the locally ~200 m thick crystal tuff unit follows an unconformity and marks the onset of intense, mainly mafic to intermediate, calc-alkaline magmatic activity. Triassic volcanic activity in the North Pamir was coeval with the major phase of Cimmerian intrusive activity in the Karakul-Mazar arc-accretionary complex to the south, caused by northward subduction of the Paleo-Tethys. It also coincided with the emplacement of basanitic and carbonatitic dikes and a thermal event in the South Tien Shan, to the north of our study area. Evidence for arc-related magmatic activity in a back-arc position provides strong arguments for back-arc extension or transtension and basin formation. This puts the Qimgan succession in line with a more than 1000 km long realm of extensional Triassic back-arc basins known from the North Pamir in the Kyrgyz Altyn Darya valley (Myntekin formation), the North Pamir of Tajikistan and Afghanistan, and the Afghan Hindukush (Doab formation) and further west from the Paropamisus and Kopet Dag (Aghdarband, NE Iran).

1. Introduction

A long history of subduction, collision, and terrane accretion shaped the Pamir salient in the Alpine-Zagros-Himalayan orogenic system (Figure 1) (e.g., [1–4]). The pre-Cenozoic portion of the Pamir orogen was significantly deformed by the Cenozoic collision of India and Asia. Preexisting structures and anisotropies along Asia's southern margin played an important role during the collision [5]. Therefore, a profound knowledge of pre-Cenozoic components in the Pamir orogen is crucial for a holistic view of deformation processes lasting until today. Northward subduction of the Paleo-Tethyan lithosphere took place along the southern margin of Asia during the Permo-Triassic. This was the interval

FIGURE 1: Regional geography of the Pamir and surrounding areas. In color: outline of the Permian Tarim LIP (orange) in the Tarim basin (yellow). Segments of the South Tien Shan are in blue letters. A: Atbashy range; P: Pobeda massif. Black box outlines the position of Figure 2.

between two major orogenic events: (1) the late Carboniferous to early Permian Hercynian orogeny of Central Asia, which closed the Turkestan Ocean and parts of the Paleo-Tethys (e.g., [6–10]), and (2) the Late Triassic Cimmerian orogeny, caused by the accretion of Gondwana derived microcontinents to Asia's southern margin (e.g., [2, 11–14]).

In this study, we aim to characterize the stratigraphic relationship, age, and magmatic genesis of the Permo-Triassic volcano-sedimentary sequence of the Chinese NE Pamir. Geochemical investigations, particularly on rocks of the bimodal Upper Triassic volcanic sequence, are used to test their genetic linkage and their connection to Triassic magmatic activity in the Karakul-Mazar volcanic arc and are regarded in context with other Permo-Triassic magmatic centers in the region. A comprehensive overview of Permian and Triassic magmatic activity in the Hindukush, the North Pamir, the Tarim basin, and the Tien Shan is presented. We hypothesize that an ~1000 km long extensional back-arc domain extended from the Chinese NE Pamir through the Hindukush and Paropamisus mountain ranges of Afghanistan into the Kopet Dag mountains of NE Iran.

2. Geological Setting of the Pamir

The Pamir has been subdivided into 3 major tectonic units, the North, Central, and South Pamir [2, 6, 15], separated by intervening suture zones (Figure 2). The North Pamir is composed of rocks associated with a Carboniferous oceanic arc that accreted to the Paleo-Asian margin in the late Carboniferous to Permian due to closure of a part of the Paleo-Tethys [3, 4, 9, 16]. This process, along with the closure of the Turkestan Ocean, further north, is regarded as the Hercynian orogeny in Central Asia [8, 17]. Major parts of the Tien Shan were consolidated during that period, with accretion of oceanic crust along multiple subduction zones [7, 18–25]. Ongoing convergence of the Paleo-Asian margin with the Karakum and Gissar blocks in the west and the Tarim craton in the east resulted in a phase of high pressure metamorphism of oceanic and continental units. Eclogite facies peak metamorphic conditions were reached by 328–319 Ma, and exhumation subsequently occurred by 303–295 Ma (Atbashy range, South Tien Shan, e.g., [24, 26]). Post-Hercynian, Permian tectonics in Central Asia were dominated by large scale strike slip faulting (e.g., [27–30]).

The Carboniferous volcanic arc of the North Pamir can be subdivided into the eastern Oytag segment, with more primitive island arc volcanic rocks and associated plagiogranites (tonalites and trondhjemites), and the western Darvaz segment, comprising pre-Carboniferous metasedimentary rocks in the Kurguvad-Faizabad zone (also named the Kurguvad block) and Carboniferous basalts and associated granodioritic rocks of continental arc affinity [3, 9, 16, 31, 32]. The Carboniferous volcanic arc system accreted in the late Carboniferous to early Permian [9]. It is bordered to the south by the Permo-Triassic Karakul-Mazar block. This block formed as an accretionary system generated by Paleo-Tethys subduction during the northward advance of the Cimmerian terranes with Gondwanan provenance—the Central and South Pamir microcontinents [11–13, 33–35]. Triassic granitoids are well known from the Karakul-Mazar block, the adjacent West Kunlun to the east, and the Badakhshan region to the west. In the Karakul-Mazar and West Kunlun, they show high-K to shoshonitic composition and typical characteristics of continental arc and syncollisional and postcollisional geotectonic settings (e.g., [36]). The closure of the Paleo-Tethys formed the Tanymas suture zone between the Central Pamir and the Karakul-Mazar block.

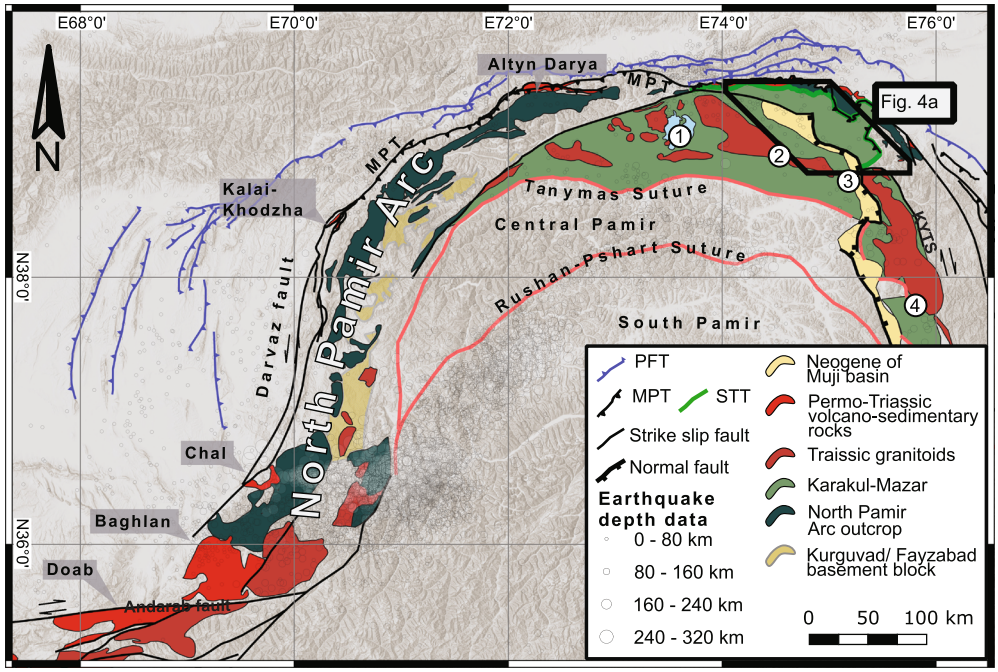

FIGURE 2: Distribution of Triassic volcano-sedimentary successions in the North Pamir and regional subdivision of the Pamir. Note that the Triassic basins are aligned along the Main Pamir Thrust (MPT) in the North. Major outcrop localities of Triassic volcano-sedimentary successions outside of our study area are named in grey boxes. Numbers indicate Triassic arc intrusions in the Karakul-Mazar and westernmost West Kunlun, from literature: (1) Karakul intrusion [2], (2) Bulunkuo and Qiate intrusions [36, 37], (3) Yuqikapa intrusion [37, 76], and (4) Muztaga and Beileki/Taer intrusions [37, 38].

Recent studies suggest that the Pamir salient formed due to deflection of Cimmerian terranes, which filled an embayment in the southern margin of the Paleo-Asian continent [5]. Intrusive complexes, associated with the Paleo-Tethys subduction, found in the Chinese northeastern Pamir have been described in detail [36–39]. However, volcanic rocks as part of a volcano-sedimentary sequence in the Chinese North Pamir have roughly similar ages, as shown in this contribution. In fact, Permo-Triassic volcano-sedimentary rocks are known to form a narrow strip along the northern edge of the North Pamir and seem to be aligned along the Main Pamir Thrust (MPT, Figure 2), which juxtaposes Paleozoic-early Mesozoic North Pamir units against sedimentary sequences of the External Pamir located in the Tarim, Alai, and Tajik Basins. Similar Permo-Triassic rock units have been described from the Hindukush in northern Afghanistan (e.g., [40]), the North Pamir of Tajikistan (e.g., [41, 42]), and Kyrgyzstan (e.g., [43, 44]).

3. Regional Permo-Triassic Volcanism

3.1. Hindukush of Afghanistan and the NW Pamir in Tajikistan and Kyrgyzstan. Permian successions of the Badakhshan area in North Afghanistan and the North Pamir of Kyrgyzstan and Tajikistan are characterized by fine-clastic and carbonate sediments (Figure 3). Several hundred-meter-thick fusulina limestones were deposited in an open marine environment on the southern shelf of the Paleo-Asian continent [45, 46]. These unconformably overlie remnants of the accreted Carboniferous arc and accreted pre-Carboniferous (meta-) sedimentary rocks [9, 46–49]. Permian volcanic rocks, mainly tuffites and epiclastic rocks, are known from the upper Permian of Afghanistan [40] and from the Darvaz range in Tadjikistan [41]. Leven et al. [41] describe basaltic and andesitic tuffs and epiclastic rocks that make up large volumes of the Kungurian and Roadian strata (corresponding to the local Tethyan Bolorian and Kubergandian Stage). Permian volcanic rocks of the NW Pamir (Darvaz range and Badakhshan) are characterized as calc-alkaline and interpreted to have erupted in an ensialic volcanic island arc [50]. The Upper Permian is characterized by relative sea level changes causing repeated uplift and erosion, followed by marine deposition. Upper Permian strata are missing in North Afghanistan [45].

The Triassic clastic sedimentation in North Afghanistan is marine and characterized by intense mafic to acidic volcanism. Weippert [51] described the superbly exposed Triassic strata in the Doab area situated on the northern flank of the Hindukush (Figures 2 and 3). The succession is subdivided into the lower (Anisian), middle (Ladinian), and upper (Carnian, Norian, Rhaetian) Doab formation. The lower Doab formation is characterized by sandstones and conglomerates, followed by shales and marls of the middle Doab formation. The upper Doab formation comprises shales, siltstones, and sandstones. Lower and Middle Triassic strata in the Doab area lack volcanic rocks. However, intermediate to acidic Anisian to Ladinian volcanism is known from other localities along the northwestern flank of the Hindukush [40, 45]. In the Doab area, intense mafic to acidic Late Triassic volcanism produced an alternation of terrigenous sandstones and basaltic, andesitic, and rhyolitic rocks. The latter yielded Norian K-Ar ages [52].

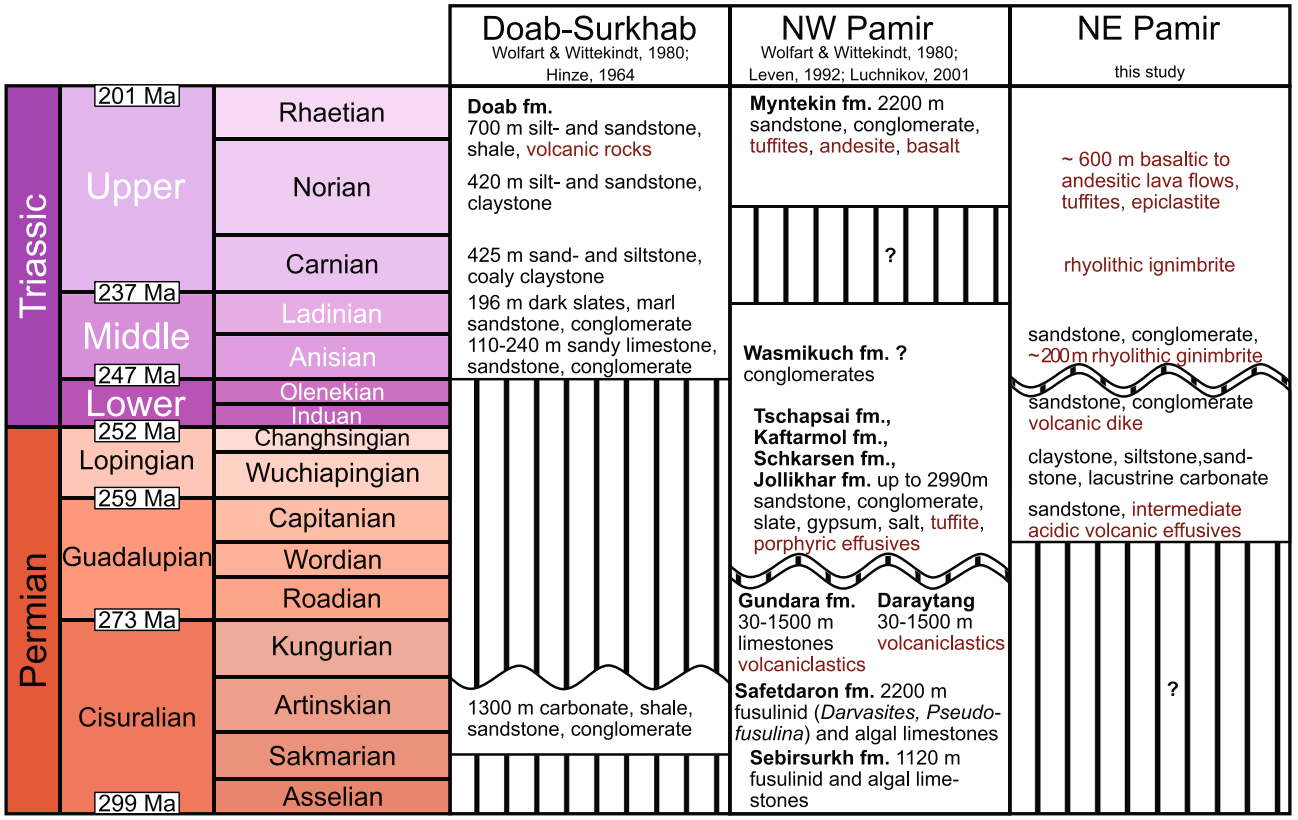

Figure 3: Simplified comparative stratigraphy of the Hindukush (Doab-Surkhab), NW Pamir, and NE Pamir strata. Wavy line marks erosional unconformities, and vertical stripes show presumed (question mark) or reported hiatus. Chronostratigraphic subdivision and rounded ages according to the International Chronostratigraphic Chart [129].

In the more recent compilations of Montenat [53] and Siehl [54], data is summarized from the North Hindukush rift. This zone of Triassic extensional basins in a back-arc position of the Paleo-Tethys subduction zone spanned from the West Hindukush into West Afghanistan (Paropamisus, e.g., [10]) and most likely further into the Aghdarband basin of the Kopeh-Dag, NE Iran [55, 56]. The Doab Formation is of the correct age, sedimentary style, and position to be viewed as part of this rift system. A direct lateral correlation is difficult, since detailed radiometric and biostratigraphic age data are sparse. Moreover, abrupt lateral facies changes hinder lithostratigraphic correlations.

Only Upper Triassic (Rhaetian) strata were described from the Altyn Darya valley in the Kyrgyz North Pamir (Figure 3). Continental clastic deposits with pyroclastic acidic and effusive intermediate to mafic rocks are grouped into the ~2500 m thick Rhaetian Myntekin formation [43, 44] and overlie Permian shallow marine strata (e.g., [41]). The Triassic succession was deposited in graben structures and is laterally highly variable. Sedimentary rocks are immature with a high proportion of volcanic clasts [43]. Luchnikov [43] compared the Myntekin Formation to similar continental Middle-to-Upper Triassic units in the area and interpreted the laterally restricted, fault-bounded, volcano-sedimentary basin to belong to a Triassic-Jurassic rift basin. Salikhov and Sakiev [50] compiled major element geochemical data and found that calc-alkaline Triassic magmatism of the North Pamir shows more complex geochemical signatures than the Permian ensialic arc magmatism. They stress an ensimatic component, interpreted as a result of short-term rear-arc extension associated with increased mantle influence.

In general, Permian sedimentary deposits are much more widely distributed than those of the Triassic strata.

3.2. Northeast Pamir. In the northeastern Chinese Pamir, the Permo-Triassic volcano-sedimentary successions have been comparatively poorly studied. Our field work focused on the Triassic rocks in the Chinese Qimgan valley (Figures 3 and 4). Our data show a coherent stratigraphic succession spanning at least the upper Guadalupian to the Cretaceous or the lower Paleogene. We also investigated a Permian deformed felsic sill in the Markansu valley, Permian andesitic to dacitic rocks in the upper Bieertuokuoyi valley, and a variety of Middle to Upper Triassic volcanic rocks in the Oytag and Gez valleys (Figure 4). The Permian units unconformably overlie Carboniferous (Hercynian) island arc-related rocks, identified as mainly basaltic to andesitic lava flows and tuffs and associated epiclastic rocks and intruded Carboniferous plagiogranites [9, 16, 31]. In the Qimgan valley, two calcite U-Pb ages from the Permian strata and one zircon U-Pb age of a crosscutting aplitic dike temporally constrain the deposition of Permian strata to between 260 and 250 Ma [9]. Rembe et al. [9] described a foraminifera-bearing limestone clast, found in a polymictic conglomerate at the base of the Permian strata, that yielded a lower Mississippian age (calcite U-Pb age 347 ± 8 Ma, MSWD = 2),

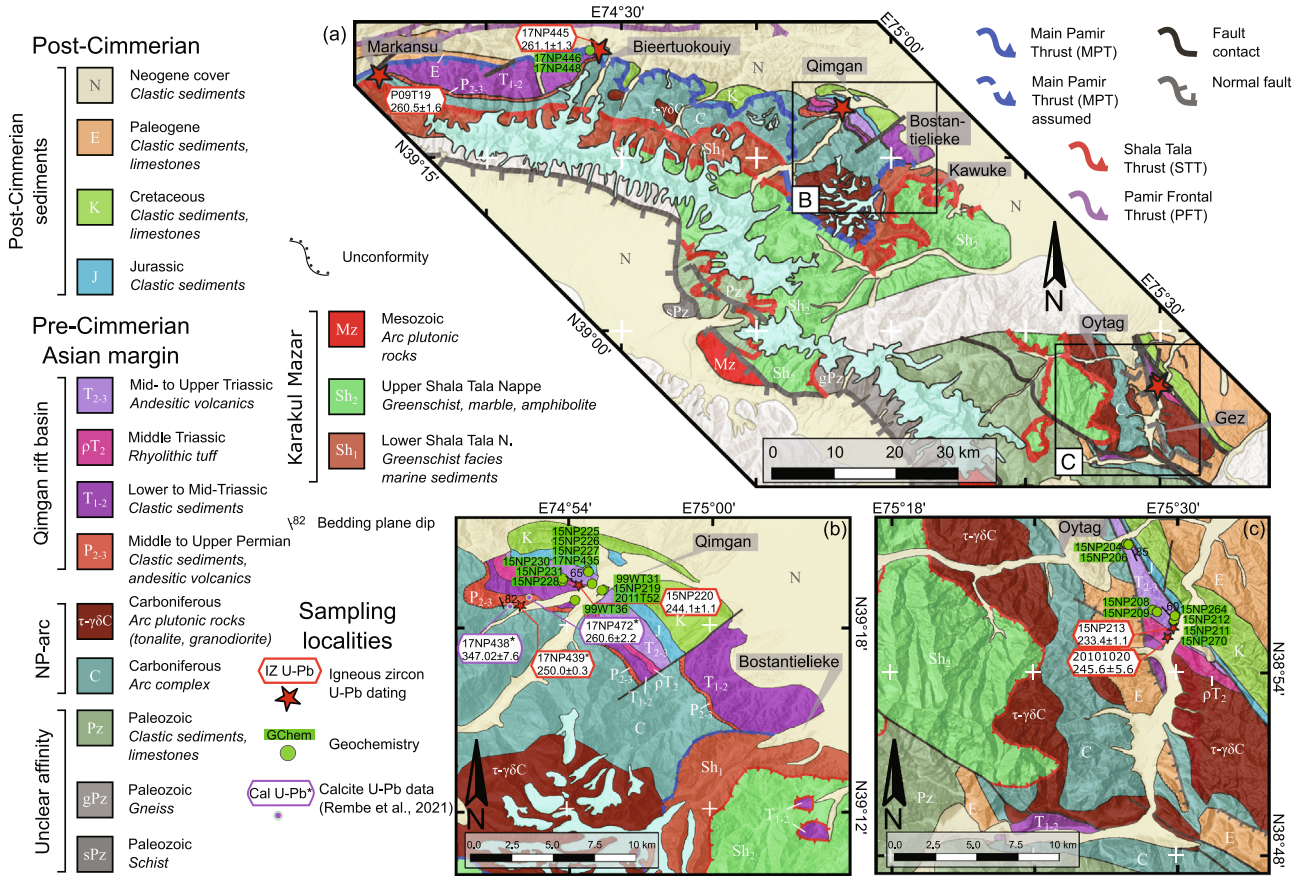

FIGURE 4: Geological map of the investigated area in the NE Pamir. Detailed maps show the distribution of geochemistry samples in the Qimgan (b) and Oytag/Gez (c) valleys and extend to Permo-Triassic strata. Both regions exhibit coherent Permo-Triassic volcano-sedimentary successions that laterally are either truncated by steep, Cenozoic faults or unconformably covered by Cenozoic sediments. Igneous zircon U-Pb age data is presented as age ± 2σ propagated error. Age data marked with an asterisk (Cal U-Pb data and data from aplitic dike sample 17NP439 in Qimgan valley) are from Rembe et al. [9].

indicating erosion of Carboniferous marine strata. An ostracod-rich lacustrine limestone from the Permian fine-grained clastic sequence gave an upper Guadalupian age (calcite U-Pb age 260 ± 2 Ma, MSWD = 3), and the crosscutting aplite yielded Lower Triassic, concordant Olenekian zircons (zircon U-Pb age 250.0 ± 0.3 Ma). Permian volcanic activity in the Qimgan succession is largely mafic to intermediate and pyroclastic, indicating high water supply in the parent magma. The abundance of volcanic rocks decreases from the base to a mid-Triassic angular unconformity which is overlain by a Middle to Late Triassic sequence of volcanic rocks. These contain a massive, several 100 m thick ignimbritic tuff layer that is covered by poorly sorted, mud-supported gravel layers. The top of the Triassic sequence is composed of a thick succession of andesitic and basaltic lava flows and tuffs.

4. Permo-Triassic Magmatic Activity in Neighboring Parts of Central Asia

4.1. The Permian Large Igneous Province in Tarim. The early Permian Large Igneous Province (LIP) in the western part of the Tarim basin is composed of large volumes of basaltic and rhyolitic rocks (e.g., [57–60]) that cover an area of about 250,000 km^2 (Figure 1). Igneous rocks of the LIP are layered mafic-ultramafic intrusions, bimodal dike swarms, granitic intrusions, kimberlites, flood basalts, rhyolites, and associated pyroclastic rock; these were emplaced in 3 major phases. Starting at ~300 Ma, diamond-bearing kimberlites intruded; these were followed by two bimodal magmatic pulses at ~290 Ma and ~280 Ma [59]. The ~290 Ma pulse marks the most widespread phase of magmatic activity in Tarim and the adjacent Tian Shan. Recently, the age of the main flood basalt eruptions has been constrained as 289.8 ± 1.0 Ma and 284.3 ± 0.4 Ma by chemical-abrasion thermal-ionization mass-spectrometry (CA-TIMS) zircon U-Pb dating [61]; these ages bracket an ~5.5 Ma long period of major mantle plume activity.

4.2. Magmatic Activity in the Tien Shan. Following the Carboniferous arc related and subsequent collisional magmatism, shortening and subduction of the Turkestan ocean and the adjacent Paleo-Tethys, the Permian period was marked by postcollisional magmatic activity in the Tien Shan (e.g., [8, 27, 29, 62]). This magmatic episode is closely linked to Permian strike-slip faulting and associated local

transtension and transpression [8, 17, 25, 28, 63–68]. In the eastern segment of the Tien Shan, postcollisional magmatism interfered with mantle plume magmatic activity of the Tarim LIP, which caused a mixed mantle-plume and postcollisional, arc-inherited, magmatism [27, 69]. The peak of the Permian postcollisional magmatic activity in the Tien Shan was reached between 290 and 280 Ma [8, 62, 70] and ceased by ~265 Ma, dated by an anatectic granite from the Pobeda massif (South Tien Shan), associated with charnockite, emplaced in a strike-slip setting [27]. Sensitive High Resolution Ion Microprobe (SHRIMP) zircon data from Permian intrusions in the Kyzylkum segment of the South Tien Shan revealed Ladinian to Norian (240–220 Ma) overgrowths on the Permian zircons, interpreted to result from elevated thermal fluxes [70]. However, Triassic magmatic rocks are relatively rare in the Tien Shan. A porphyritic dike in the Kyzylkum segment (Figure 1) of the South Tien Shan dated as 236 Ma by U-Pb on zircon was reported by Hall [71]. Small volumes of basanite dikes and pipes found in the Gissar and Alai ranges gave mica and hornblende $^{40}Ar/^{39}Ar$ ages between 256 and 237 Ma [72]. Younger, rare alkaline and carbonatitic rocks of the Alai segment in the South Tien Shan formed in a complex active continental margin extensional setting associated with mantle upwelling [73, 74]. They gave apparent ages of between 200 and 220 Ma by $^{40}Ar/^{39}Ar$ dating of mica and amphibole and phlogopite, apatite, amphibole, and whole rock Rb-Sr isochrone dating. However, high MSWD values for the Rb-Sr isochrone and forced plateau ages for the $^{40}Ar/^{39}Ar$ data require careful use of these ages.

4.3. The Triassic Intrusions of the Karakul–Mazar Arc-Accretionary Complex and the Westernmost West Kunlun. Triassic intrusive rocks have been described from the Permo-Triassic Karakul-Mazar arc-accretionary complex and the western branch of the West Kunlun, such as the Karakul intrusion [2]; the Yuqikapa intrusion [34, 75]; the Muztaga, Yuqikapa, and Taer intrusions [37]; the Beileki/Taer intrusion [38]; the Bulunkuo intrusion [76]; and the Bulunkuo, Qiate, and Yuqikapa intrusions [36] (Figure 2). Paleo-Tethys subduction might have commenced before the Permian [36]. Middle Triassic subduction and accretion lead to crustal melting and the emplacement of the Yuqikapa pluton between 245 and 243 Ma [34, 37, 75] and the calc-alkaline Qiate leucogranite at 240 Ma [36]. The mechanism for the emplacement of the high-K calc-alkaline Taer and Muztaga intrusions (234–227 Ma) is a matter of discussion and has been interpreted as the result of either delamination of thickened lithosphere [36] or slab break-off due to collision of the Karakul-Mazar block and the Central Pamir [37, 76]. A biotite granite, sampled at the northern shore of Karakul Lake within the Karakul-Mazar block, gave a similar age of 227.0 ± 4.1 Ma [2] and might be associated with this phase. Norian to Rhaetian magmatism emplaced the high-K calc-alkaline Bulunkuo granodiorite (221–219 Ma) and related Arkaz (215–213 Ma) and Mazar plutons (~209 Ma) in the West Kunlun, due to continued northward subduction of the Paleo-Tethys [36]. Collision of the Central Pamir and the Karakul-Mazar block and formation of the Tanymas-Jinsha suture happened by the Late Triassic [13, 36]. However, some authors suggest an earlier, Middle Triassic closure, based on geochemical arguments [37, 76].

5. Methods

5.1. Field Work and Sample Preparation

5.1.1. Sampling. Field work was undertaken in the northwest part of the North Pamir, ~100 km south-west of the town of Kashgar, China (Figures 1 and 2). We collected samples in seven localities (Figure 4), and detailed field work focused on the outcrops of the volcano-sedimentary Permo-Triassic sequence in the Qimgan and Gez valley areas (Figure 4(b)). The Qimgan valley exposes a largely undisturbed section of Carboniferous to Eocene strata. The Gez valley is tectonically more complex. Multiple, transecting subvertical faults hinder the correlation of Paleozoic to Paleogene strata in the field.

5.1.2. Zircon U-Pb Dating. To determine the crystallization age of igneous rocks, U-Pb isotopes were measured in zircons from five volcanic rock samples. Zircons were separated using jaw crusher, disc grinder, water table, magnetic separation, and heavy liquids (sodium polytungstate (SPT), diiodomethane (DI)). Zircons were poured onto a glass plate and arranged in lines on double-sided sticky tape under a binocular microscope. Zircons were sorted for clear appearance and size. Alignment of zircon grains in epoxy resin helps for better single-grain recognition. Mounted grains were polished to expose an internal surface and imaged with cathodoluminescence (CL) at the electron microprobe facility of the University of Potsdam.

5.1.3. Whole Rock Geochemistry and XRD. Twenty-one volcanic rock samples of fresh appearance were chosen for whole rock geochemistry. The samples were cleaned, crushed, and milled in an agate mill to a particle size <62 μm. Melt tablets for X-ray fluorescence spectroscopy (XRF) analysis to measure major and trace elements were prepared at the University of Potsdam using fluxing agent FX-X65-2 (lithium tetraborate : lithium metaborate, 66 : 34). Samples for rare earth elements (REE), yttrium, and scandium analysis were sintered with sodium peroxide at 480°C and dissolved in hydrochloric acid. REE plus scandium and yttrium were then separated in ion exchange columns. Powder tablets were prepared from 10 samples to determine the mineral composition by X-ray powder diffraction (see Table 1).

5.2. Analytical Work

5.2.1. Zircon LA-ICP-MS U-Pb Dating. 207 zircon grains from five volcanic rock samples were analyzed. Zircon U-Pb dating from all but one sample (20101020-3) was done according to the parameters described in Rembe et al. [9] and Zhou et al. [77]. Laser ablation of samples 17NP445, P09T19, 15NP220, and 15NP213 was accomplished with an ASI RESOlution 193 nm ArF excimer laser system at the Radiogenic Isotope Facility (RIF), The University of

Table 1: Sample description.

Sample	Rock	Purpose	Mineralogy in TS	Mineralogy from XRD	Latitude (N)	Longitude (E)
			Markansu and Bieertuokouyi valley			
P09T19	Deformed felsic sill	IZ-UPb	—	—	39.3688	74.0494
17NP445	Rhyolite	IZ-UPb	Compare 17NP446	—	39.4053	74.4569
17NP446	Rhyolite	TS, GC	gm-kfsp-hem	—	39.4053	74.4569
17NP448	Intermediate tuff	TS, GC	fsp-cal-lv-gm	—	39.40642	74.448821
			Qimgan valley			
15NP219	Basaltic andesite	GC	—	—	39.31897	74.92573
15NP225	Basaltic andesite	TS, GC	plg-gm	plg-qz-hem-mnt-sa-cal	39.32964	74.91448
15NP226	Basaltic andesite	TS, GC	plg-gm-opk	—	39.32882	74.91501
15NP227	Basalt	TS, GC	plg-gm-cpx	ab-cal-qz-hem-clc-bt	39.3287	74.91522
15NP228	Dacitic dike	TS, GC	plg-gm-kfsp-cpx	qz-clc-hd-sa-ab-hem	39.32125	74.89802
15NP230	Rhyolitic tuff	TS, GC	gm-kfsp-plg-qz-mca-opk	qz-hem-ab-or-bt-clc	39.32508	74.89732
15NP231	Rhyolitic tuff	TS, GC	qz-plg-gm-kfsp-mca-opk	—	39.32508	74.89732
2011 T52	Basalt	TS, GC	plg-gm-aug	an-qz-cal-mnt	39.3187134	74.9246562
99WT31	Basaltic andesite	TS, GC	plg-gm-opk	—	39.322222	74.917778
99WT36	Andesite	GC	—	—	39.313333	74.905833
15NP220	Rhyolitic tuff	IZ-UPb	Compare 15NP230	—	39.3215	74.9084
17NP475	Rhyolitic tuff	TS, IZ-UPb	gm-kfsp-plg-qz-mca-chl	—	39.32166	74.881959
17NP435	Intermediate ignimbrite	TS,GC	gm-pmc	—	39.322977	74.905659
			Oytag and Gez valley			
15NP264	Basaltic andesite	TS, GC	plg-opk-gm-aug	aug-an40-mnt-hem-ilm-qz	38.93077	75.49877
15NP204	Andesite	GC	—	qz-ab-or-kln-dol	38.97001	75.46497
15NP206	Basaltic andesite	GC	—	ab-clc-mag-dol-nsn	38.9696	75.4664
15NP208	Andesite	TS, GC	gm-plg	—	38.93393	75.48344
15NP209	Basalt	TS, GC	plg-gm	—	38.93287	75.4864
15NP211	Basalt	TS, GC	plg-gm-cpx-hbl	qz-cal-kln-hem-hd-ap	38.92758	75.49801
15NP212	Tuff	TS, GC	plg-gm-lth	qz-cal-sd-kln-hem-str	38.92799	75.49825
15NP270	Basaltic andesite	TS, GC	plg-gm-opk	—	38.93031	75.50143
20101020-3	Rhyolite	IZ-UPb	—	—	38.9188	75.4938
15NP213	Rhyolite	IZ-UPb	—	—	38.924	75.4978

Mineral abbreviations are according to Siivola and Schmid [130]. gm: ground mass; pmc: pumice; opk: opaque mineral; lth: xenolith.

Queensland. Laser spot size was 30 μm. For each ablation spot, 3 s of blank was collected, followed by 20 s of ablation and 5 s of washout. Zircons were carefully examined using CL images to place ablation spots. Fractures and zones with strongly differing Th/U values were identified and excluded. Using He carrier gas at a flow rate of 0.35 l/min and adding N_2 gas for sensitivity enhancement, the gas mixture from the laser chamber was transferred to the plasma torch of a Thermo iCAP RQ quadrupole ICP-MS with 0.85 l/min Ar nebulizer gas. The ICP-MS signals were optimized by signal tuning before starting data acquisition.

The following isotopes were counted (dwell time in brackets): ^{88}Sr (0.005 s), ^{91}Zr (0.001 s), ^{200}Hg (0.01 s), ^{204}Pb (0.01 s), ^{206}Pb (0.045 s), ^{207}Pb (0.055 s), ^{208}Pb (0.01 s), ^{232}Th (0.01 s), and ^{238}U (0.01 s). Data reduction was done in the program Iolite v2.5, which runs within the Igor Pro environment [78, 79] using the Vizual Age [80] data reduction scheme. Each five unknowns were bracketed by the standard zircon 91500 with a ^{206}Pb/^{238}U age of 1062.4 ± 0.4 Ma (2σ) and ^{206}Pb/^{207}Pb age of 1065.4 ± 0.3 Ma (2σ) [81]. Temora 2 zircons (^{206}Pb/^{238}U age of 416.78 ± 0.33 Ma (2σ) [82]) where treated as unknowns. The primary standard gave a ^{206}Pb/^{238}U age of 1062.7 ± 0.2 Ma (σ) and Temora 2 gave a ^{206}Pb/^{238}U age of 420.7 ± 0.2 Ma (2σ) in the measurement session. All unknowns were filtered for concordance and strontium content.

Sample 20101020-3 was measured at the University of Potsdam using a Thermo Scientific Element 2 ICP-MS coupled to a CETAC LSX 213 nm Nd:YAG laser. The laser spot size was set to 25 μm. Cathodoluminescence images were used to locate the laser spots on the zircon grains. All analyses were normalized to the GJ-1 zircon standard [83–85] to correct for laser-induced elemental fractionation and mass discrimination by the instrument. Zircon GJ-1 yielded a ^{206}Pb/^{238}U age of 602.9 ± 6.6 Ma (2σ). The published weighted ID-TIMS ^{206}Pb/^{207}Pb age of GJ-1 is 608.53 ± 0.37 Ma (2σ) with ^{206}Pb/^{238}U ages varying from 596.2 to 602.7 Ma [83]; the ^{206}Pb/^{238}U age of this standard remains

problematic, as discussed recently in Schaltegger et al. [85]. Schaltegger et al. [85] present an ID-TIMS $^{206}Pb/^{238}U$ age of 600.28 ± 0.16 Ma (2σ). This is in agreement with our measurement. Data reduction was done in the program UranOS v.2.02 [86] similar to the procedure described in Bande et al. [87].

Analytical 1σ-uncertainties of the samples measured at the Radiogenic Isotope Facility laboratory at The University of Queensland are mostly below 1%; the analysis performed at the University of Potsdam had a higher uncertainty of about 3%. We expanded the analytical uncertainty, as suggested by Horstwood et al. [88] by propagating a total systematic uncertainty of 0.4% (2σ) into the population age, containing the long-term variance of the $^{206}Pb/^{238}U$ signal measured on secondary zircon standard Temora 2, the accuracy of the measurement of primary zircon standard 91500, and the uncertainty of the ^{238}U decay constant. For sample 20101020-3, we propagated a total systematic uncertainty of 0.9% (2σ), containing the accuracy of the measurement of zircon standard GJ-1 and the uncertainty of the ^{238}U decay constant.

All results were handled in the statistics program R, version 3.6.0 [89]. We used the IsoplotR package version 3.6 [90] to calculate and visualize age data. To derive meaningful sample ages, we applied the concordia distance filter (d_c) as presented by Vermeesch [91]. We defined discordance threshold values for igneous zircon samples as $-1 < d_c < 5$.

5.2.2. XRF and ICP-AES Whole Rock Geochemistry. Analyses by XRF (X-ray fluorescence spectroscopy) were done at the GeoForschungsZentrum Potsdam (GFZ) on a PANalytical AXIOS Advances XRF system. Analyses of international reference materials were used for calibrations. Monitor samples and 130 certified reference materials were used for the correction procedures. The detection limit of the XRF system is generally 10 ppm. The rare earth elements plus yttrium and scandium were measured by inductively coupled-plasma atomic-emission-spectroscopy (ICP-AES) at the University of Potsdam on an Agilent ICP5100 machine following the procedure of Zuleger and Erzinger [92]. Long-term precision for ICP-AES at the University of Potsdam is generally <5%. High field strength elements were measured at the GFZ using standard ICP-MS procedures [93, 94]. The detection limit is generally ±5% [95]. Concentrations of H_2O and CO_2 were determined on 20 mg of sample powder, weighed in tin foil using a Euro EA 3000 Elemental Analyser at UP. Geochemical data was handled in R 3.6.0 [89], using the GCDkit package version 6.0 [96].

5.2.3. XRD Analysis. Mineral analyses of 10 volcanic rock samples were obtained at UP using a PANalytical Empyrean powder X-ray diffractometer (XRD) with a Bragg-Brentano geometry. The XRD is provided with a PIXcel1D detector using Cu K_α radiation ($\lambda = 1.5419$ Å) operating at 40 kV and 40 mA. θ/θ scans were run in a 2θ range of 4–70° with step size of 0.0131° and a sample rotation time of 1 s. It was equipped with a programmable divergence and antiscatter slit and a large Ni-beta filter. The detector was set to continuous mode with an active length of 3.0061°. The total detection time was 21 min.

6. Results

6.1. Field Work and Petrography. In the Lower Guadalupian to Lower Triassic strata of the succession, volcanic rocks are basaltic to andesitic, fine- to coarse-grained pyroclastic rocks, with locally occurring lava flows and dikes. They are interlayered with or intrude mainly fine-clastic, dark greenish grey volcanomictic sediments. In the well-exposed Qimgan succession, the basal, fine-grained clastic sedimentary units trend into coarse-grained, red sandstones and conglomerates. Rare aphyric, greenish-grey dikes and sills penetrate the volcano-sedimentary strata. The effusive rocks appear dark grey to greenish grey in hand specimens and form up to 2 m thick laterally traceable beds (Figure 5(a)). In the upper Bieertuokuoyi valley, we sampled a pale red, up-to 20 m thick rhyolite with feldspar phenocrysts of almost 1 cm for geochemistry and zircon U-Pb dating. It was sampled close to the estimated basal contact with the underlying Carboniferous rocks (Figure 5(b)), which is covered by alluvial fans in this location. In the Qimgan section study area, pyroclastic rocks (many aphyric) dominate over lava flows. In some volcanic rocks, small (<1 cm) plagioclase phenocrysts were observed. Distinctive lapilli tuff layers are also present (Figure 5(c)). Aphyric lava flows in contact with mudstones formed peperites (Figure 5(d)).

Microscopic textures typical of magma mingling, such as partially resorbed quartz crystals and sieve-textured feldspar, were observed from the pale red rhyolite in the upper Bieertuokuoyi valley (Figure 5(e)). The abundant tuff layers, found in the lower part of the Qimgan section, typically show small, fragmented plagioclase and quartz crystals, volcanic and sedimentary lithic fragments, and perlitic glass fragments (Figure 5(f)). The matrix in all sampled tuffs is altered, and pseudomorphs of glass shards are rare.

In the upper, coarse-grained clastic unit of the Qimgan section, two brick-red crystal tuff layers were identified. Zircons, for U-Pb dating, were not present in collected tuff samples; thus, the age estimates for the coarse clastic unit remain unclear. Since it is discordantly overlain by Mid-Triassic volcanic rocks (Figure 6(a)), it might be Lower to lower Middle Triassic. In the Lower to lower Middle Triassic units, sandstones and conglomerates form up to several meters thick, partly amalgamated beds that laterally persist over hundreds of meters. Besides the two crystal tuff layers, several aphyric, dark greenish dikes were found. A red, crystal-rich, up-to-~200 m thick ignimbrite (Figure 6(b)) forms the base of the Middle to Upper Triassic unit. Welded, accretionary lapilli tuff layers (Figure 6(c)) were observed along the top of the ignimbrite. After some tens of meters of coarse, matrix-supported conglomerates, an approximately 600 m thick package of poorly stratified basaltic to andesitic lava flows, associated tuffs, and epiclastic breccias was found. This unit was the main target for geochemistry and is present not only in the Qimgan valley but also in the Gez and Oytag valleys (Figures 4(b) and 4(c)), where it is crosscut by multiple transpressive faults associated with the Kashgar-Yecheng-Transfer fault system (KYTS, Figure 2). Amongst the Upper Triassic mafic to intermediate volcanic rocks, lava flows with plagioclase, pyroxene, and/or

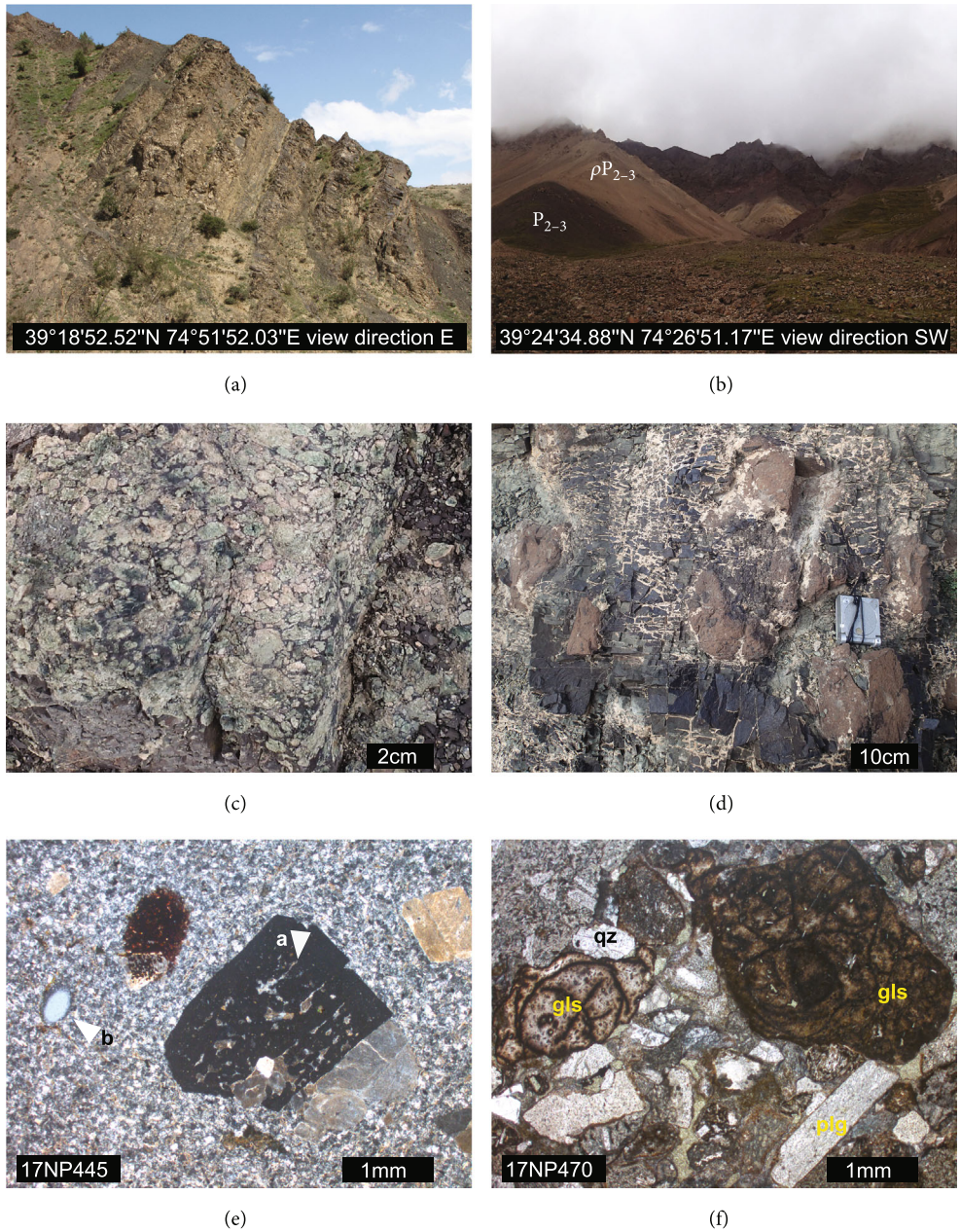

FIGURE 5: Permian volcanic rocks crop out as fine- to coarse-grained volcaniclastic deposits and lava flows in the Qimgan valley ((a) bed thickness ~1–2 m) and the upper Bieertuokuoyi valley (b). The pale rose rhyolite (ρP_{2-3}) in (b) yielded an age of 261.1 ± 1.3 Ma. It is accompanied by volcaniclastic and epiclastic deposits (P_{2-3}). The contact with the underlying Carboniferous rocks is obscured by massive alluvial fans. Permian aphyric and less often phyric tuffs and lapilli tuffs in the Qimgan valley (c). The presence of various tuffs and peperite textures (d) indicates high water supply to the magmatic system and the interlayered sediments. The greenish mudstone in (d) was affected by contact metamorphism and turned into brittle hornfels, showing a different fracture behavior than the intruding brownish volcanic rock. In the thin section of rhyolite sample 17NP445 ((e) cross-polarized light) from the upper Bieertuokuoyi valley, we found evidence for magma mingling, such as sieve textures in feldspar (white arrow (a)) and resorption of quartz (white arrow (b)). Thin sections of the fine-grained pyroclastic rocks, here from tuff sample 17NP470 ((f) plane-polarized light), show fragmented quartz (qz) and plagioclase (plg) crystals and abundant perlitic glass fragments (gls).

amphibole phenocrysts are common. Large hornblende-phyric andesites were observed not only in the Qimgan valley but also in Upper Triassic volcanic rocks from the Altyn Darya valley. Plagioclase forms as glomerocrysts in some basaltic andesites (e.g., Figure 6(f)). The mafic to intermediate Upper Triassic volcanic sequence is likely Carnian to Rhaetian in age; however, it was not dated radiometrically. The age estimate is based on the age of the underlying ~200 m thick Ignimbrite, presented in this study, and the age of the overlying amagmatic, fine- to coarse-grained, and lower Jurassic conglomeratic beds. Jurassic strata in all outcrop areas typically have several coal seams; these are mined in the Gez valley.

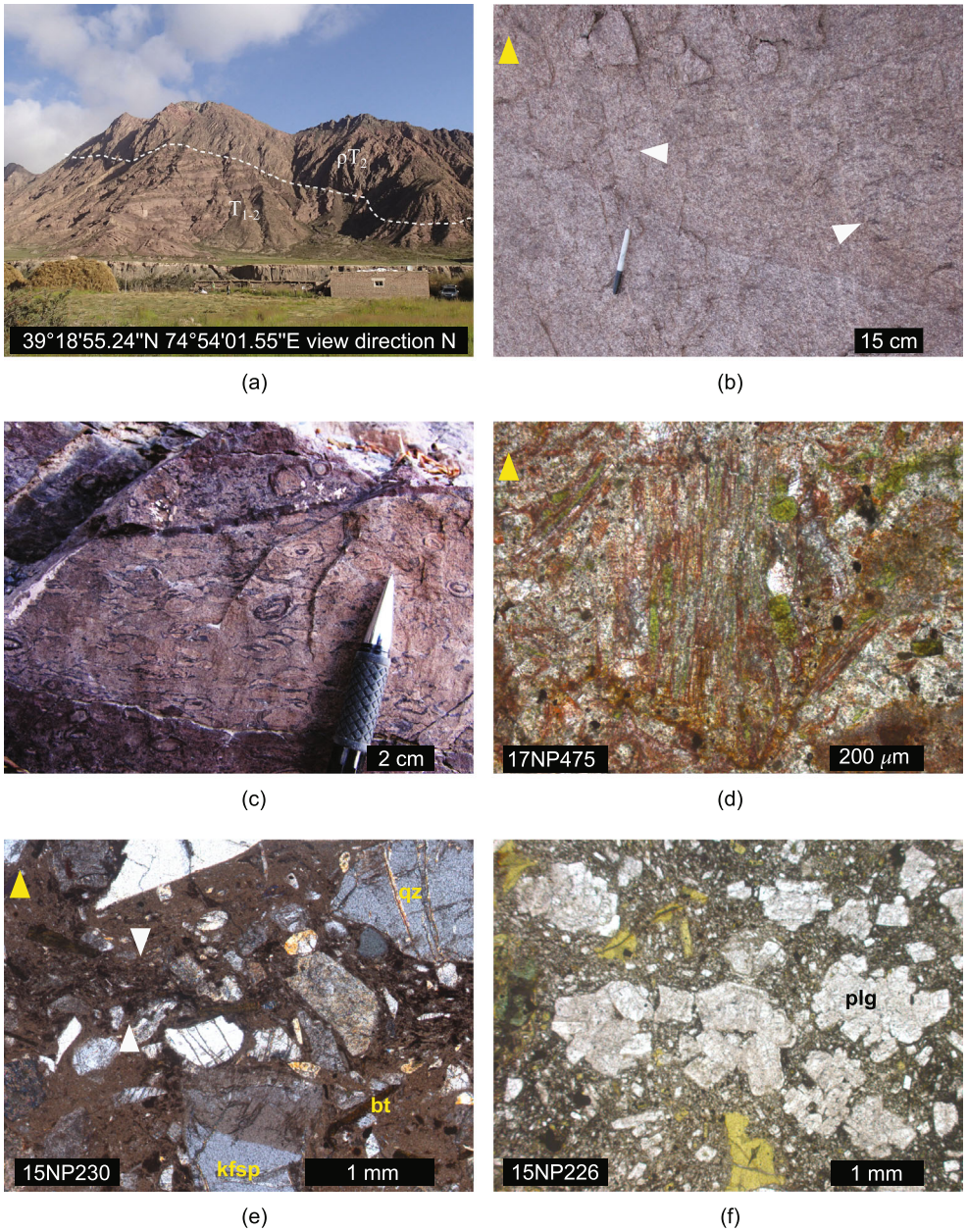

FIGURE 6: Triassic volcanic rocks crop out in the Chinese Qimgan valley (a); the distinct angular unconformity (white dashed line) separates the Middle Triassic (ρT_2) red ignimbritic crystal tuff from the underlying ($T_{1\text{-}2}$) red sandstone and conglomerate beds. The medium-grained crystal-rich tuff (b) is characterized by homogenous crystal size and pale grey fiamme (white arrow). At the top of the ~200 m thick ignimbrite, a layer of welded accretionary lapilli was found (c). Two distinct, brick-red, unwelded crystal tuff layers were found interbedded with the red clastic sediments below the unconformity. They show elongate pumice fragments ((d) plane-polarized light) and lack zircons. Thin-section photograph of the ignimbritic crystal tuff showing welded pumice (between white arrows) that forms fiamme textures ((e) cross-polarized light). Phenocrysts are fragmented potassium feldspars (kfsp) and quartz (qz); the latter show frequent fracturing. Biotite (bt) appears as brownish green flakes. The basalts, basaltic andesites, and andesites from the Middle to Upper Triassic are generally more phyric than the Permian mafic to intermediate rocks. Thin section ((f) plan-polarized light) shows glomerophyric plagioclase. Yellow arrows in (b, d, e) indicate upward direction.

6.2. Age Determination. An age overview of the five samples dated for this study is given in Table 2, and supplementary material Table A lists the single grain U-Pb isotope data.

We report two ages for each sample: (1) the youngest concordant single grain age (±2σ propagated uncertainty) and (2) the age of the youngest coherent group of concordant grains (±2σ propagated uncertainty), with a probability value of greater than 0.2, calculated by the peak fit algorithm of IsoplotR [90]. For the calculation of both ages, we used a discordance cut-off range of $-1 < d_c < 5$ (relates to $-3 < d_r = 1 - ([^{206}Pb/^{238}U]/[^{207}Pb/^{206}Pb]) < 15, 98$), where d_c is the concordia distance as defined by Vermeesch [97] and

Table 2: LA-ICP-MS igneous zircon U-Pb age data.

Sample	Rock type	Location	Latitude	Longitude	Age[1] of youngest concordant single grain [Ma] ± 2σ (prop)	Age[1] of youngest coherent group of concordant grains (peak fit, [90]) [Ma] ± 2σ (prop)	Number of grains
15NP213	Rhyolite	Gez valley	38.924	75.4978	228.6 ± 2.0	233.4 ± 1.1	44
15NP220	Welded crystal tuff	Qimgan valley	39.3215	74.9084	219.4 ± 2.7	244.1 ± 1.1	89
17NP445	Rhyolite	Bieertuokouyi valley	39.4053	74.4569	244.1 ± 2.6	261.1 ± 1.3	23
20101020-3	Crystal tuff	Gez valley	38.9188	75.4938	244 ± 16	246 ± 11	20
P09T19	Felsic sill	Markansu valley	39.3688	74.0494	236.9 ± 3.7	260.5 ± 1.6	31

[1]Discordance filter is $-1 < d_C < 5$.

implemented in IsoplotR 3.6. The concordia distance is a modified version of the Aitchison distance discordance filter d_a and considers the correlated uncertainties of the U-Pb isotope pairs. Generally, we prefer peak fit ages (age (2)) as population ages for interpretation. This takes into account the problem that single concordant grains may be mathematically seemingly concordant due to their large age error [98] or due to the minimal distance between concordia and discordia line for young isotope gain or loss. Since in our data set age (1) and age (2) differ partly by tens of millions of years, which we interpret as the result of lead loss (left-skewed age distribution curve, [98]), we decided to present both ages in Table 2 for a more complete view on the age distribution.

6.2.1. Ages of Volcanic Rocks. Starting in the western most outcrop area (Figure 4), dacitic sill sample P09T19 from the Markansu river valley and reddish rhyolite sample 17NP445 from upper Bieertuokuoyi gave similar peak fit ages of 260.5 ± 1.6 Ma and 261.1 ± 1.3 Ma, respectively (Figures 7(a) and 7(b)). They are sampled close to the base of the Permo-Triassic Basin. Further to the east, we sampled an ignimbritic crystal-tuff cropping out in the Qimgan and the Gez valley. We dated 89 zircons from sample 15NP220 taken in the Qimgan valley and obtained a peak fit age of 244.1 ± 1.1 Ma for the youngest coherent group of concordant grains and an age of 219.4 ± 2.7 Ma for the youngest concordant single grain (Figures 7(c) and 7(f)). Sample 20101020-3 from the Gez valley yielded an age of 246 ± 11 Ma for the youngest coherent group of concordant grains and a similar age of 244 ± 16 Ma for the youngest concordant single grain (Figure 7(d)). The peak fit ages of both samples overlap within 2σ age uncertainty. Sample 15NP213—a crystal-tuff, sampled close to the location of 20101020-3—gave a peak fit age of 233.4 ± 1.1 Ma (Figure 7(e)). The new ages together with the age of an aplitic dike at the base of the Qimgan basin of 250.0 ± 0.3 Ma [9] imply a volcanic phase that lasted from at least the Capitanian to the Carnian (~261–233 Ma).

6.3. Geochemistry

6.3.1. Whole Rock Geochemistry. We analyzed 21 volcanic rock samples for major and trace element concentrations mainly derived from Middle to Upper Triassic strata. Trace element values were normalized against primitive mantle [99], and REE were normalized against chondrite [100]. Samples 17NP446 and 17NP448 are from the Permian strata, and sample 99WT36 is from the Upper Permian to Lower Triassic strata in the Qimgan valley (Figure 4). They are plotted and interpreted along with the Middle to Upper Triassic samples (supplementary material Table B). Three analyses (of samples 17NP448, 15NP211, and 15NP212) yielded very high LOI values between 12.4 wt% and 25.5 wt% and very low SiO_2 values of 44.9 wt% and 25.6%, respectively. They are regarded as substantially altered and were handled cautiously and excluded from discrimination plots. The remaining 18 samples are basic to acid rocks with SiO_2 concentrations between 48.4 and 74.6. MgO concentrations are low to moderate between 0.4 wt% and 6.8 wt%, K_2O values range between 0.2 wt% and 5.0 wt%, and Al_2O_3 values are high, between 13 and 21 wt%. TiO_2 concentrations are generally low, ranging from 1 wt% in the basic to intermediate rocks to 0.2 wt% in the rhyolitic samples. All samples have low Zr (44 to 286 ppm) and low Y (2.3 to 53 ppm) content. A pronounced positive Pb/Pb* anomaly with values between 1.4 and 4.6 ($Pb/Pb^* = Pb_N/\ sqrt(Ce_N{}^*Pr_N)$) correlates with a negative Ti/Ti* anomaly with values between 0.2 and 1 ($Ti/Ti^* = Ti_N/sqrt\ (Eu_N{}^*Dy_N)$).

All samples show petrographic and/or geochemical (LOI) indications for alteration. However, plotted in the diagram of Ohta and Arai [101] (Figure 8(a)), none of the 18 samples with moderate or low LOI diverges far from the unaltered rock trajectory. Sample 17NP435 (similar to high LOI samples 15NP211 and -212) has a Na_2O value below detection limit and for this reason was not plotted in the diagram (Figure 8(a)), assuming that Na_2O was removed by secondary processes.

The investigated mafic to intermediate samples can be classified as basalt, basaltic andesite, and andesite with some trachytic equivalents. Acid rocks are classified as dacites and rhyolites following Le Bas et al. [102] (Figure 8(b)). Acid volcanic rocks are peraluminous whereas intermediate and mafic volcanic rocks are mainly metaluminous.

Some of the mafic to intermediate samples have low, tholeiitic K_2O values between 0.19 wt% and 0.58 wt%.

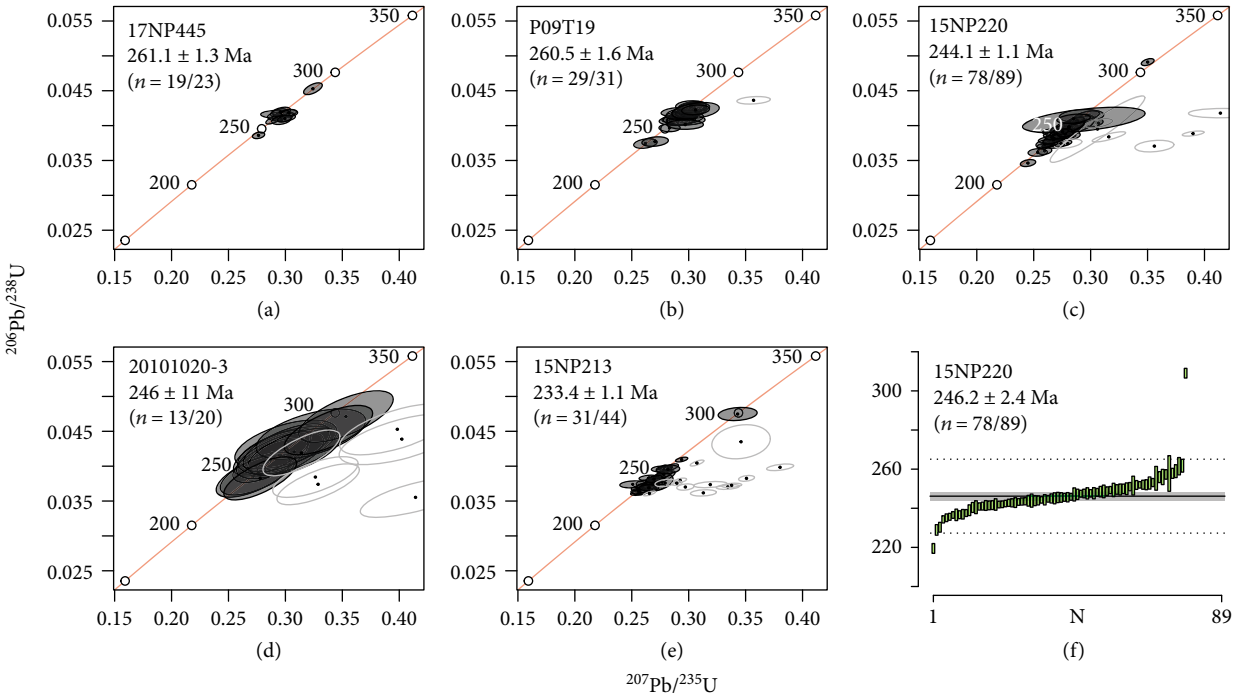

FIGURE 7: Wetherill plots of the zircon U-Pb age data for Permo-Triassic rocks from the upper Bieertuokuoyi valley (a), the Markansu valley (b), the Qimgan valley (c, f), and the Gez valley (d, e). Error ellipses are colored translucent grey; stacking of multiple ellipses will result in darker grey to black shades. Excluded, discordant error ellipses are plotted unfilled. The ages in (a–e) are peak fit ages ± 2σ (prop.); the age in (f) is a weighted mean age ± 2σ.

Intermediate and acid samples show a higher scatter and can be classified as tholeiitic to even high-K calc-alkaline according to the scheme of Peccerillo and Taylor [103] (Figure 8(c)). Plotted in the Na_2O+K_2O-CaO diagram of Frost et al. [104] (not shown), two trends can be distinguished: a calcic and an alkali-calcic trend.

Since the concentration of alkaline elements and MgO or CaO may be changed during alteration [105–107], the use of more immobile elements for classification is helpful. Ti and V concentrations show a calc-alkaline trend (Figure 8(d)) as defined by Shervais [108]. This contradicts the classification of the mafic rocks as tholeiitic using the K_2O-SiO_2 diagram. Potassium mobility is a very common secondary effect in volcanic rocks (e.g., [105, 106]); therefore, we regard the rocks as calc-alkaline.

Using the Zr-Ti diagram of Pearce [109], mafic volcanic rock samples plot in the Island Arc Lava field (Figure 8(e)), and in the MnO-TiO-P_2O_5 ternary diagram of Mullen [110], mafic to intermediate rocks plot within the continental arc basalt (COB) and island arc tholeiite (IAT) fields (Figure 8(f)). We used the Sc/Ni vs. La/Yb diagram presented by Bailey [111] to classify orogenic andesitic rocks. The andesites have low Sc/Ni ratios and moderate La/Yb ratios and plot in the continental island arc field (Figure 8(g)). These classifications suggest a close linkage to arc magmatic processes.

Total REE+Y concentrations are between 50 and 187 ppm. Light REE are enriched over heavy REE with $(La/Lu)_N$ values ranging between 2 and 9. Heavy REE show a flat chondrite-normalized pattern in mafic rock samples, suggesting a low-P spinel mantle source (Figure 9(a)). The outliers are two rhyolitic samples (17NP446, 15NP228) with anomalously low heavy REE pattern (Figure 9(b)). A progressively pronounced negative Eu anomaly develops from basalts to rhyolites, typical for plagioclase fractionation. Eu/Eu* values range between around 1 in the basic to intermediate samples and 0.3 for the Middle Triassic Qimgan rhyolitic ignimbrite.

6.3.2. XRD Analysis. XRD analyses largely agree with petrography. Results show clinopyroxene as augite and hedenbergite. XRD analyses also classified common fine-grained groundmass and alteration minerals (Table 1). Calcite, hematite, and clay minerals (montmorillonite and kaolinite) are dominant secondary minerals.

7. Discussion

7.1. The Permo-Triassic North Pamir Basin in the Regional Geodynamic Setting

7.1.1. Ages of Magmatic Activity. The Permo-Triassic magmatic phase in the North Pamir spans at least ~28 Ma, from the Permian Capitanian stage into the Upper Triassic Carnian stage (~261–233 Ma). A thick pile of hitherto undated basic to intermediate rocks that overlies the rhyolitic crystal tuffs (~244–233 Ma) in Qimgan and Gez might extend this time span further into the Upper Triassic. The whole succession is conformably overlain by amagmatic, coal-bearing Jurassic clastic sediments. Next, we present a compilation

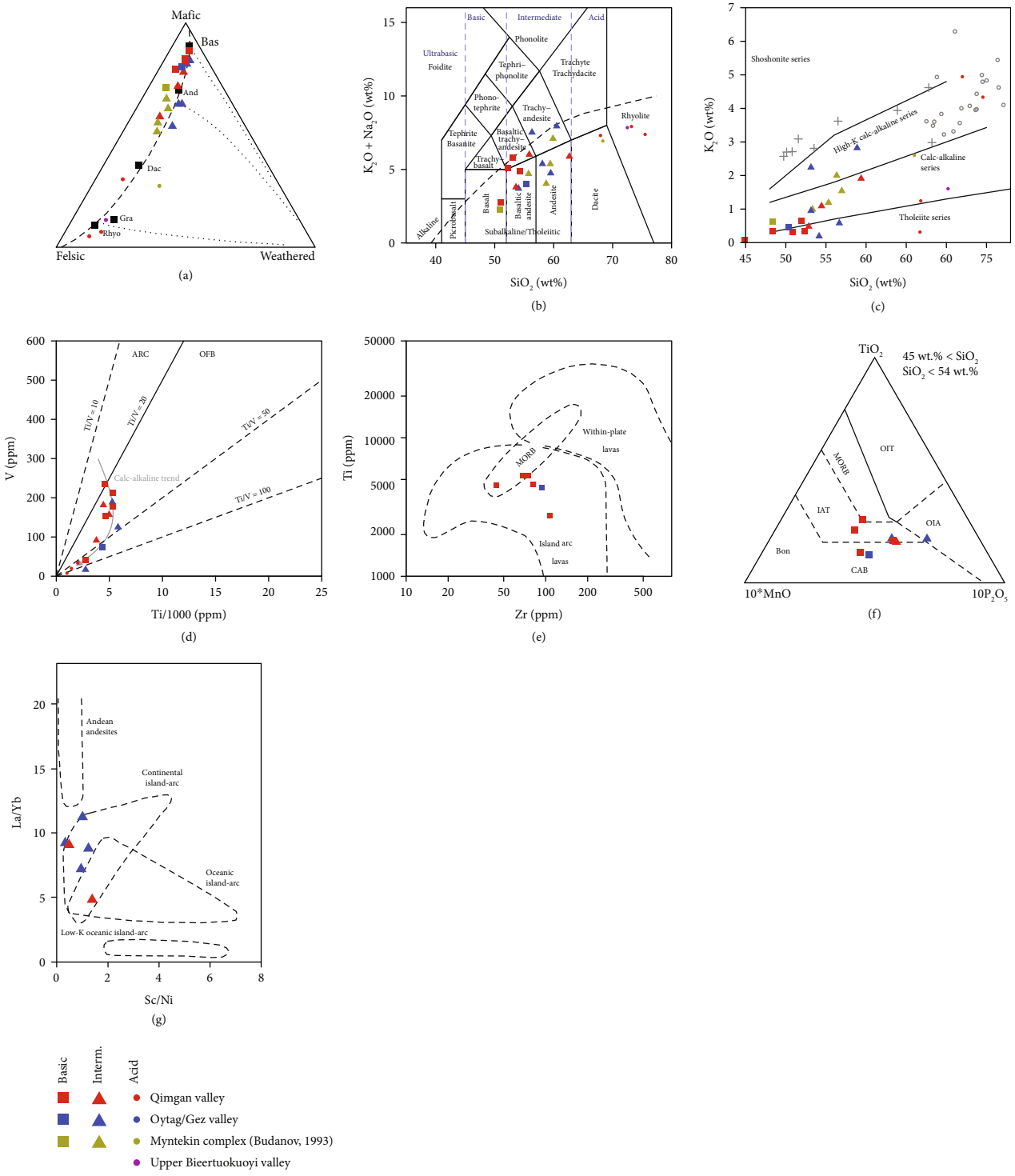

FIGURE 8: Geochemical characterization of Permo-Triassic volcanic rocks of the North Pamir. Note that literature data from the Myntekin formation [44] is plotted along with newly presented samples in (a–c). (a) All sampled rocks plot close to the trajectory defined by fresh volcanic rocks in the Felsic-Mafic-Weathered ternary diagram developed by Ohta and Arai [101]. (b) According to the TAS diagram [102], the samples classify as basalts, basaltic andesites, andesites, and their trachytic equivalents. Acidic rocks are classified as dacites and rhyolites that plot in the tholeiitic to high-K calc-alkaline series (c) according to the classification of Peccerillo and Taylor [103]. Data from intrusive rocks ("o") and their mafic enclaves ("+") from the Karakul Mazar and West Kunlun are plotted for comparison [2, 37, 38, 76]. In the Ti/1000 against V diagram (d), the samples show a calc-alkaline trend, as defined by [108]. This matches well with a classification of the basic rocks as island arc lavas (e) according to the diagram of Pearce [109] and as island-arc tholeiites and continental arc basalts (f) according to the classification of Mullen [110]. In the Sc/Ni vs. La/Yb plot of Bailey [111], andesitic rocks are mainly identified as continental island arc andesites (g).

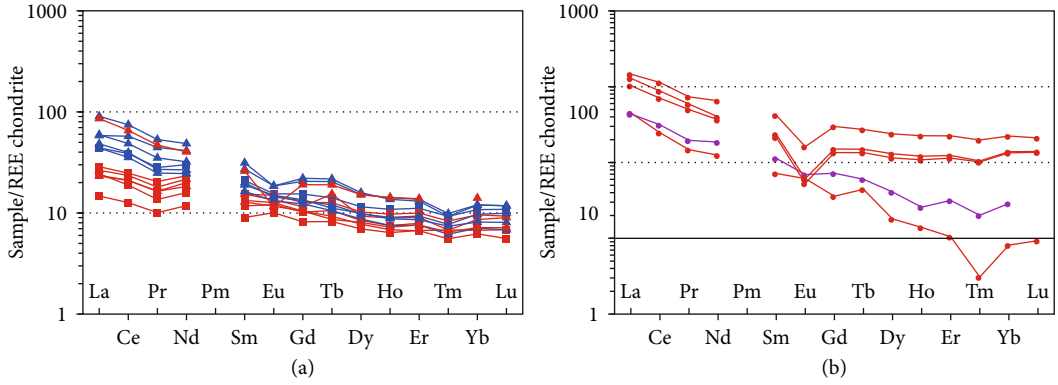

FIGURE 9: Rare earth elements (REE) normalized to C1-chondrite [100] of the Permo-Triassic volcanic sequence: basic to intermediate rocks (a) show moderately enriched light REE and no moderate Eu/Eu* anomaly. Acid rocks (b) show more pronounced Eu/Eu* anomaly and more enriched light REE. Two samples (17NP446 and 15NP228) show anomalous REE pattern with less enriched light REE and low heavy REE concentration. Flat heavy REE element pattern of mafic rocks demonstrates shallow parental magma differentiation above the garnet stability field.

of magmatic events during the Permo-Triassic in Central Asia that explores a possible linkage based on the synchroneity and geodynamic settings.

In the *Tien Shan*, Permian magmatic activity close to the North Pamir is correlated with a Hercynian late- to postcollisional transcurrent geodynamic setting that activated large NW-SE and ENE-WSW wrench faults [25, 27, 28, 68]. The Permo-Triassic North Pamir volcanism postdates the major phase of magmatic activity in the Tien Shan (295–275 Ma [8]). However, extensional tectonics in the North Pamir, forming back-arc basins, partly overlaps with the late stages of Hercynian postcollisional transcurrent tectonics in the Tien Shan. It is beyond the scope of this study to determine whether the Permo-Triassic basin formation in the North Pamir was ruled by pure extensional or transtensional tectonics. The temporal coincidence with large-scale transcurrent faulting in the nearby Tien Shan during the Permian makes an overall transcurrent geodynamic setting also in the North Pamir likely. It coincides with local magmatic activity connected to strike-slip faulting and ongoing exhumation in the North, Northeast, and South Tien Shan north of Tarim (e.g., 296–260 Ma Narat range [8]; 267 Ma alkaline granite, Gissar segment [18]; 287–266 Ma anatectic granite, Pobeda massif, Kokshaal segment [27]). The vast majority of Hercynian postcollisional magmatism in the Tien Shan ceased at that time (e.g., [7, 70]), making a direct genetic linkage to the North Pamir volcanic rocks unlikely. Triassic volcanism in the North Pamir correlates with a high temperature event recorded in the Kyzylkum segment (240–220 Ma [70]), Late Permian to Triassic basanitic dikes from the Gissar and Alai segments [72], and Late Triassic alkaline and carbonatitic intrusions in the Alai segment of the South Tien Shan [73, 74]. Geochemical data from the 220 Ma carbonatites and alkaline gabbro presented in Vrublevski et al. [73] indicate their intrusion in an extensional active continental margin setting. However, the Middle to Late Triassic was a phase of relative tectonic quiescence and widespread erosion in the Tien Shan [112].

The *Tarim LIP* volcanism was partly coeval and interfered with Hercynian postcollisional igneous activity in the Tien Shan. Activity in the Tarim LIP terminated in the Cisuralian (e.g., [59]). Recent high-precision ages of the major flood basalt units put a younger limit of about 284 Ma on the magmatism [61]. Hence, the LIP clearly predates the volcanic rocks found in the Chinese North Pamir.

Evidence for Permian magmatism in the *Karakul-Mazar* arc-accretionary complex is scarce and restricted to the ~250 Ma Kayizi pluton of the West Kunlun [113]. This arc-related magmatic activity, however, continued into the Triassic and is widespread in the nearby West Kunlun range. Middle to Upper Triassic calc-alkaline, arc-related volcanism in the North Pamir coincides with major intrusive activity in the Karakul-Mazar domain, suggesting a plausible correlation.

It must be stated, however, that the geodynamic situation of the North Pamir during the Permian remains relatively vague, as little is known about the geochemical compositions of the Permian volcanic rocks in the Hindukush and the North Pamir. We argue that a genetic link to the north-vergent Paleo-Tethys subduction, which might have been active during that time [36], is likely. Crustal extension in the North Pamir, forming the upper plate of the Paleo-Tethys subduction zone, could also have been driven by slab retreat of the downgoing Paleo-Tethys slab (Figure 10). Trench migration towards the south could also explain the relatively wide Karakul-Mazar accretionary complex. However, steep subduction of a cold oceanic slab alone (not requiring rollback) is capable of causing back-arc extension (e.g., [114]).

7.1.2. Petrogenesis of the Triassic Volcanic Rocks and Implications for a Permo-Triassic Cimmerian Extensional Back-Arc System. Middle to Late Triassic rocks show calc-alkaline trends typical for volcanic arcs (Figure 8). Andesites show features such as low Al_2O_3, TiO_2, Zr, and Y content characteristic for collisional andesites as defined by Bailey [111]. These are classified as continental island arc andesites based on their La/Yb and Sc/Ni ratios (Figure 8(g)), which ties them to coeval arc volcanic rocks of the Karakul-Mazar arc-accretionary complex to the south. Accordingly, trace elements of the volcanic rocks compared to the intrusive rocks of the Karakul-Mazar arc-accretionary complex show similar LILE enrichment with respect to HFSE, a

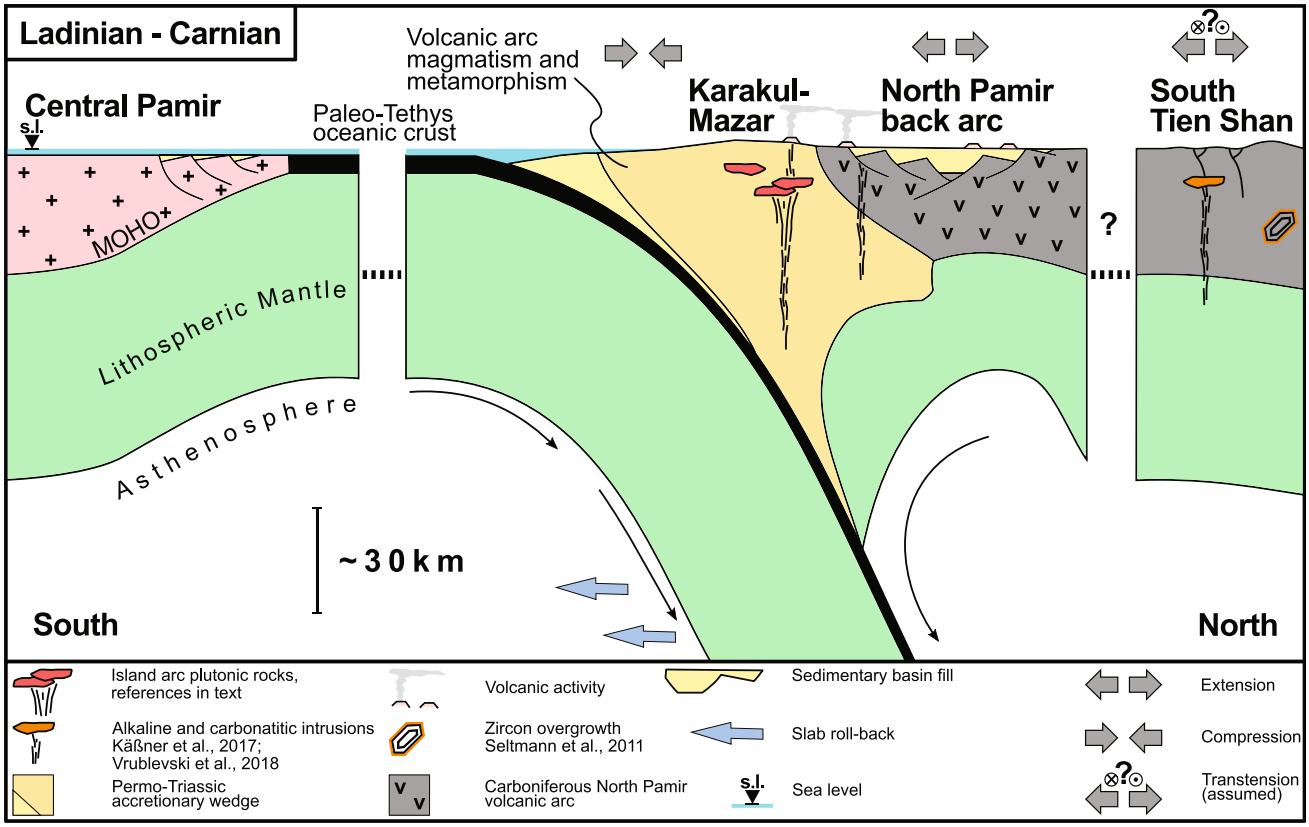

FIGURE 10: Reconstruction of the situation along the South-Asian margin in the Ladinian to Carnian, during deposition of the Middle to Upper Triassic volcaniclastic unit. The Karakul-Mazar arc-accretionary complex forms along the subduction zone of the Paleo-Tethys ocean. In the back-arc, extension creates space for the sedimentation of Permian and Triassic volcano-sedimentary strata. During that time, potentially ongoing transtensional tectonics [28] in the South Tien Shan may have provoked the emplacement of alkaline melts [72, 73] and zircon overgrowths [70]. Large parts of Central Asia experienced erosional or nondepositional conditions during this interval.

pronounced Pb-positive anomaly and a Ti-negative anomaly (Figure 8). This is indicative of the influence of slab-derived volatiles during melt generation in a subduction zone. The flat heavy REE pattern of the mafic volcanic rocks indicate melt production in a shallow spinel-bearing mantle. We compared Sm/Yb and Dy/Yb from the Qiate (~240 Ma) and Bulunkuo (221–219 Ma) intrusions [36] with the Qimgan and Gez Triassic volcanic suite (Figure 11). In general, low ratios, especially in mafic volcanic rocks, are indicative of melts that formed above the garnet stability field [115], in an area of normal, nonthickened continental crust. The Middle to Upper Triassic rocks of the Qimgan and Gez valley have ratios that resemble those of the Bulunkuo intrusion (Figure 11). Those findings challenge the idea of the pre-Cimmerian (and pre-Cenozoic) cratonic Tarim-Tajik crust below the North Pamir (cratonic Asia), as was hypothesized by previous studies [116, 117].

The volcano-sedimentary Permo-Triassic sequence in Qimgan and Gez must be interpreted in context with the Karakul-Mazar arc-accretionary complex in the framework of the Paleo-Tethys subduction along the southern Asian continental margin prior and during the Cimmerian orogeny. Back-arc formation can be associated with the production of a variety of magma types [118–120], and arc-like volcanic rocks underline the genetic linkage of the back-arc basin volcanics and the Karakul-Mazar arc. The temporal and geochemical correlation with volcanic rocks of the volcano-sedimentary Myntekin complex [44] and a continuation of the Permo-Triassic volcano-sedimentary suite from the northeastern North Pamir into the Afghan Badakhshan and Hindukush areas and further into the Paropamisus and Kopet Dag in NE Iran (e.g., [53–55, 121, 122]) trace a more than 1000 km long zone of (Permo-)Triassic back-arc extension to the north of the Paleo-Tethys subduction zone. It connects the North Hindukush rift with the Myntekin Formation in the Altyn Darya valley and the Triassic Qimgan and Gez suite. Indicators of high thermal fluxes, alkaline, and carbonatitic melt formation in the South Tien Shan, west of the Talas Fergana fault [70, 72–74], and evidence for strike-slip activity [28] suggest a wide zone affected by extension and transtension in the Middle-Late Triassic (Figure 10).

From the Kungurian onwards, there is evidence for deposition of volcaniclastic material in a back-arc basin of the Paleo-Tethys subduction zone in the region [10, 40, 41, 50]. Back-arc sedimentation and volcanism intensified in the Triassic, forming multiple, connected back-arc basins (e.g., [53, 54]). However, a more precise geochemical classification of the Permian volcanic suites in the Hindukush and North Pamir is needed to demonstrate that volcanic arc and

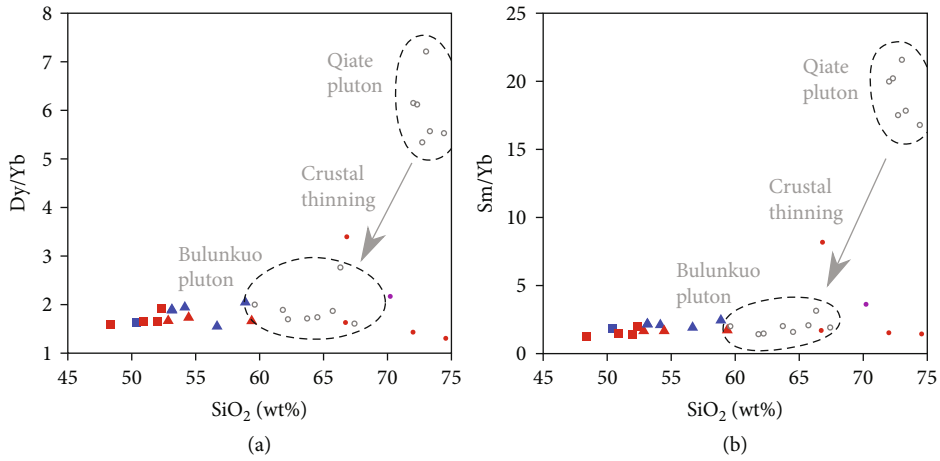

FIGURE 11: Volcanic rocks of the Qimgan and Gez suite show low Dy/Yb (a) and Sm/Yb (b) ratios similar to values derived from the Upper Triassic Bulunkuo intrusion (Qiate and Bulunkuo values taken from Chen et al. [36]).

back-arc activity continued from the Permian into the Triassic. Regardless of the uncertainties arising from missing geochemical data, the newly described Permo-Triassic units from the northeast North Pamir must be seen in line with aforementioned areas, as they share the same age, island arc affinity and geodynamic position close to the Paleo-Tethys subduction zone.

7.2. Implications for the Modern Pamir. The shape of the present-day Pamir has frequently been discussed. The existence of linear facies belts along a paleo-Asian margin prior to the collision with India has been a major argument for an indentation of Indian lithosphere and ~300 km northward displacement of the Pamir with respect to Tibet [1, 123]. Recently, a preexisting embayment along the Paleo-Asian margin was postulated, significantly reducing the amount of shortening accommodated in the Pamir [5, 9]. The major constituents of the North Pamir are the Carboniferous North Pamir volcanic arc, the Permo-Triassic volcano-sedimentary back-arc basin, and the Karakul-Mazar-derived Shala Tala nappe (e.g., [33]). The Main Pamir Thrust (MPT), a likely Miocene thrust system (e.g., [124]), forms the northern border of the North Pamir (Figure 2). It juxtaposes Paleozoic and Mesozoic units of the North Pamir against Mesozoic to Cenozoic units of the External Pamir. Shallow, active seismicity is documented from the northern margin of the North Pamir and the External Pamir fold and thrust belt (Figure 2, e.g., [125–128]). Remnants of the Permo-Triassic back-arc basin are found all along the fault trace of the MPT. They are mainly positioned in the hanging wall (e.g., Upper Bieertuokuoyi, Altyn Darya) but also in the foot wall (Qimgan). We propose that crustal heterogeneities in the Hercynian crust (North Pamir volcanic arc), weakened by Triassic back-arc extension, might have facilitated the nucleation of the MPT, thus codetermined Cenozoic deformation. The width of the basin, possibly decreased by the MPT, is crucial for a shortening estimation along that large scale fault structure. From the geochemical data collected from the Middle and Upper Triassic in Qimgan and Gez, we infer a relatively low magnitude of extension, since geochemistry of the volcanic rocks shows continental island-arc character. There is no evidence for ocean floor spreading and associated MORB magmatism.

8. Conclusion

The upper Bieertuokuoyi, Qimgan, and Gez volcano-sedimentary suite was deposited between ~260 Ma (Capitanian) and ~233 Ma (Carnian), possibly continuing into the late Upper Triassic. The Permo-Triassic Basin formed on top of the Carboniferous North Pamir volcanic arc that accreted during the Hercynian orogeny to the southern margin of Asia. Volcanic rocks were emplaced throughout the Permo-Triassic in a back-arc position with respect to the north-vergent Paleo-Tethys subduction zone, and magmas were derived from noncratonic crust (spinel stability field) in close vicinity to the continental arc in the Karakul-Mazar and West Kunlun realms. Our new data, interpreted in context with published findings from the NW Pamir, and the Badakhshan and Hindukush ranges, allows us to connect the volcano-sedimentary sequences from the North Hindukush rift, the Myntekin formation, and the Qimgan-Gez suite to form an ~1000 km long North Hindukush–North Pamir extensional or transtensional back-arc zone. A Middle-Late Triassic extension-related thermal imprint and volcanism in the South Tien Shan can be correlated. The presence of a Permo-Triassic extensional domain to the north of the Paleo-Tethys subduction zone might have facilitated northward thrusting in the North Pamir during the Cimmerian orogeny. However, we argue that reactivation of preexisting structures and inhomogeneities—related to that rift—during the Cenozoic is likely, since all outcrops of the Permo-Triassic extensional basin are well aligned along the Miocene Main Pamir Thrust of the North Pamir.

Data Availability

All data used for this study can be found in supplementary tables, Table A (containing U-Pb isotope data) and Table B (containing whole rock major and trace element data),

which are uploaded to UQ eSpace (https://doi.org/10.48610/ff37708, run by The University of Queensland).

Conflicts of Interest

The authors declare that they have no conflicts of interest.

Acknowledgments

We thank Langtao Liu for help with field work. For support during laboratory work, we thank Christine Fischer and Christina Günther. We also thank Martin Timmermann and Uwe Altenberger for helpful discussions on geochemical data. This research has been supported by the Deutsche Forschungsgemeinschaft (grant nos. SO 436/12-1 and KL 495/27-1) and the Deutscher Akademischer Austauschdienst (grant no. 2016001932). Open-access publishing was funded by the Deutsche Forschungsgemeinschaft (DFG, German Research Foundation)—projekt number 491466077.

References

[1] V. S. Burtman and P. H. Molnar, *Geological and geophysical evidence for deep subduction of continental crust beneath the Pamir*, Geological Society of America, 1993.

[2] M. Schwab, L. Ratschbacher, W. Siebel et al., "Assembly of the Pamirs: age and origin of magmatic belts from the southern Tien Shan to the southern Pamirs and their relation to Tibet," *Tectonics*, vol. 23, no. 4, 2004.

[3] M. L. Bazhenov and V. S. Burtman, "The kinematics of the Pamir arc," *Geotectonics*, vol. 16, 1982.

[4] S. Ruzhentsev, I. Pospelov, and A. N. Sukhanov, "Tectonics of Khalaihumb-Sauksau zone of the North Pamir," *Geotectonics*, vol. 4, pp. 68–80, 1977.

[5] Y.-P. Li, A. C. Robinson, M. Gadoev, and I. Oimuhammadzoda, "Was the Pamir salient built along a Late Paleozoic embayment on the southern Asian margin?," *Earth and Planetary Science Letters*, vol. 550, article 116554, 2020.

[6] M. L. Bazhenov and V. S. Burtman, "Tectonics and paleomagnetism of structural arcs of the Pamir-Punjab syntaxis," *Journal of Geodynamics*, vol. 5, no. 3-4, pp. 383–396, 1986.

[7] D. Konopelko, Y. S. Biske, K. Kullerud et al., "Early Carboniferous metamorphism of the Neoproterozoic South Tien Shan-Karakum basement: new geochronological results from Baisun and Kyzylkum, Uzbekistan," *Journal of Asian Earth Sciences*, vol. 177, pp. 275–286, 2019.

[8] Y. S. Biske, D. L. Konopelko, and R. Seltmann, "Geodynamics of late Paleozoic magmatism in the Tien Shan and its framework," *Geotectonics*, vol. 47, no. 4, pp. 291–309, 2013.

[9] J. Rembe, E. R. Sobel, J. Kley, R. Zhou, R. Thiede, and J. Chen, "The Carboniferous arc of the North Pamir," *Lithosphere*, vol. 2021, article 6697858, no. 1, 2021.

[10] J. Boulin, "Hercynian and Eocimmerian events in Afghanistan and adjoining regions," *Tectonophysics*, vol. 148, no. 3-4, pp. 253–278, 1988.

[11] J. He, P. Kapp, J. B. Chapman, P. G. DeCelles, and B. Carrapa, "Structural setting and detrital zircon U–Pb geochronology of Triassic–Cenozoic strata in the eastern Central Pamir, Tajikistan," *Geological Society, London, Special Publications*, vol. 483, no. 1, pp. 605–630, 2019.

[12] A. C. Robinson, M. Ducea, and T. J. Lapen, "Detrital zircon and isotopic constraints on the crustal architecture and tectonic evolution of the northeastern Pamir," *Tectonics*, vol. 31, no. 2, 2012.

[13] D. P. Villarreal, A. C. Robinson, B. Carrapa et al., "Evidence for Late Triassic crustal suturing of the Central and Southern Pamir," *Journal of Asian Earth Sciences*, no. article 100024, 2019.

[14] D. B. Imrecke, A. C. Robinson, L. A. Owen et al., "Mesozoic evolution of the eastern Pamir," *Lithosphere*, vol. 11, no. 4, pp. 560–580, 2019.

[15] P. Matte, P. Tapponier, N. Arnaud et al., "Tectonics of Western Tibet, between the Tarim and the Indus," *Earth and Planetary Science Letters*, vol. 142, no. 3-4, pp. 311–330, 1996.

[16] J. Rembe, R. Zhou, E. R. Sobel et al., "Calcite U–Pb dating of altered ancient oceanic crust in the North Pamir, Central Asia," *Geochronology*, vol. 4, no. 1, pp. 227–250, 2022.

[17] Y. S. Biske and R. Seltmann, "Paleozoic Tian-Shan as a transitional region between the Rheic and Urals-Turkestan oceans," *Gondwana Research*, vol. 17, no. 2-3, pp. 602–613, 2010.

[18] D. Konopelko, R. Seltmann, Y. Mamadjanov et al., "A geotraverse across two paleo-subduction zones in Tien Shan, Tajikistan," *Gondwana Research*, vol. 47, pp. 110–130, 2017.

[19] D. V. Alexeiev, Y. S. Biske, A. V. Djenchuraeva, A. Kröner, and O. F. Getman, "Late carboniferous (Kasimovian) closure of the South Tianshan Ocean: no Triassic subduction," *Journal of Asian Earth Sciences*, vol. 173, pp. 54–60, 2019.

[20] J. R. Worthington, P. Kapp, V. Minaev et al., "Birth, life, and demise of the Andean-syn-collisional Gissar arc: Late Paleozoic tectono-magmatic-metamorphic evolution of the southwestern Tian Shan, Tajikistan," *Tectonics*, vol. 36, no. 10, pp. 1861–1912, 2017.

[21] D. V. Alexeiev, Y. S. Biske, B. Wang et al., "Tectono-stratigraphic framework and Palaeozoic evolution of the Chinese South Tianshan," *Geotectonics*, vol. 49, no. 2, pp. 93–122, 2015.

[22] C. Loury, Y. Rolland, B. Cenki-Tok, P. Lanari, and S. Guillot, "Late Paleozoic evolution of the South Tien Shan: insights from P-T estimates and allanite geochronology on retrogressed eclogites (Chatkal range, Kyrgyzstan)," *Journal of Geodynamics*, vol. 96, pp. 62–80, 2016.

[23] C. Loury, Y. Rolland, S. Guillot et al., "Crustal-scale structure of South Tien Shan: implications for subduction polarity and Cenozoic reactivation," *Geological Society, London, Special Publications*, vol. 427, no. 1, pp. 197–229, 2017.

[24] C. Loury, Y. Rolland, S. Guillot et al., "Tectonometamorphic evolution of the Atbashi high-P units (Kyrgyz CAOB, Tien Shan): implications for the closure of the Turkestan Ocean and continental subduction–exhumation of the South Kazakh continental margin," *Journal of Metamorphic Geology*, vol. 36, no. 8, pp. 959–985, 2018.

[25] A. Jourdon, C. Petit, Y. Rolland et al., "New structural data on Late Paleozoic tectonics in the Kyrgyz Tien Shan (Central Asian Orogenic Belt)," *Gondwana Research*, vol. 46, pp. 57–78, 2017.

[26] M. Satybaev, L. Ding, A. Takasu et al., "Petrology of metamorphic rocks from the Atbashy complex, Southern Tien-Shan, Kyrgyzstan," *Geoscience Frontiers*, vol. 9, no. 6, pp. 1795–1807, 2018.

[27] C. Loury, Y. Rolland, P. Lanari et al., "Permian charnockites in the Pobeda area: implications for Tarim mantle plume activity and HT metamorphism in the South Tien Shan range," *Lithos*, vol. 304-307, pp. 135–154, 2018.

[28] Y. Rolland, D. V. Alexeiev, A. Kröner, M. Corsini, C. Loury, and P. Monié, "Late Palaeozoic to Mesozoic kinematic history of the Talas-Ferghana strike-slip fault (Kyrgyz West Tianshan) as revealed by $^{40}Ar/^{39}Ar$ dating of syn-kinematic white mica," *Journal of Asian Earth Sciences*, vol. 67-68, pp. 76–92, 2013.

[29] D. Konopelko, G. Biske, R. Seltmann, O. Eklund, and B. Belyatsky, "Hercynian post-collisional A-type granites of the Kokshaal Range, southern Tien Shan, Kyrgyzstan," *Lithos*, vol. 97, no. 1-2, pp. 140–160, 2007.

[30] M. M. Buslov, Y. Fujiwara, K. Iwata, and N. N. Semakov, "Late paleozoic-early Mesozoic geodynamics of Central Asia," *Gondwana Research*, vol. 7, no. 3, pp. 791–808, 2004.

[31] Y.-H. Jiang, S.-Y. Liao, W.-Z. Yang, and W. Z. Shen, "An island arc origin of plagiogranites at Oytag, western Kunlun orogen, northwest China: SHRIMP zircon U-Pb chronology, elemental and Sr-Nd-Hf isotopic geochemistry and Paleozoic tectonic implications," *Lithos*, vol. 106, no. 3-4, pp. 323–335, 2008.

[32] L. Kang, P. X. Xiao, X. F. Gao, W. Chao, Y. Zaichao, and X. Rengang, "Geochemical characteristics, petrogenesis and tectonic setting of oceanic plagiogranites belt in the northwestern margin of western Kunlun," *Acta Petrologica Sinica*, vol. 31, no. 9, pp. 2566–2582, 2015.

[33] A. C. Robinson, "Mesozoic tectonics of the Gondwanan terranes of the Pamir plateau," *Journal of Asian Earth Sciences*, vol. 102, pp. 170–179, 2015.

[34] A. C. Robinson, A. Yin, C. E. Manning, T. M. Harrison, S. H. Zhang, and X. F. Wang, "Tectonic evolution of the northeastern Pamir: constraints from the northern portion of the Cenozoic Kongur Shan extensional system, western China," *Geological Society of America Bulletin*, vol. 116, no. 7, pp. 953–973, 2004.

[35] L. Angiolini, A. Zanchi, S. Zanchetta, A. Nicora, and G. Vezzoli, "The Cimmerian geopuzzle: new data from South Pamir," *Terra Nova*, vol. 25, no. 5, pp. 352–360, 2013.

[36] S. Chen, H. Chen, K. Zhu, and Y. Tao, "Petrogenesis of the Middle–Late Triassic S- and I-type granitoids in the eastern Pamir and implications for the Tanymas–Jinshajiang Paleo-Tethys Ocean," *International Journal of Earth Sciences*, vol. 110, pp. 1213–1232, 2021.

[37] Y.-H. Jiang, R.-Y. Jia, Z. Liu, S. Y. Liao, P. Zhao, and Q. Zhou, "Origin of Middle Triassic high-K calc-alkaline granitoids and their potassic microgranular enclaves from the western Kunlun orogen, Northwest China: a record of the closure of Paleo-Tethys," *Lithos*, vol. 156-159, pp. 13–30, 2013.

[38] J. Huang, R. Yang, J. Yang, and C. Cui, "Geochemical characteristics and tectonic significance of Triassic granite from Taer region, the northern margin of West Kunlun," *Acta Geologica Sinica-English Edition*, vol. 87, no. 2, pp. 346–357, 2013.

[39] Q. Zhang, Y. Liu, Z. Wu, H. Huang, K. Li, and Q. Zhou, "Late Triassic granites from the northwestern margin of the Tibetan Plateau, the Dahongliutan example: petrogenesis and tectonic implications for the evolution of the Kangxiwa Palaeo-Tethys," *International Geology Review*, vol. 61, no. 2, pp. 175–194, 2019.

[40] C. Hinze, "Die geologische Entwicklung der östlichen Hindukush-Nordflanke (Nordost-Afghanistan)," in *Zur Geologie von Nordost-und Zentral-Afghanistan*, D. Wirtz, C. Hinze, G. Gabert, and L. Benda, Eds., pp. 19–75, 1964.

[41] E. J. Leven, T. B. Leonova, and V. Y. Dmitriev, "Perm'Darvaz-Zaalaiskoi zony Pamira. Fuzulinidy, ammonoidei, stratigrafiya (the Permian system in the Darvaz-Transalai zone of Pamir: fusulines, ammonoids, stratigraphy)," *Rossiyskaya Akademiya Nauk, Trudy Paleontologicheskogo Instituta*, vol. 253, pp. 1–204, 1992.

[42] V. N. Krestnikov, "History of the geological development of the Pamirs and adjacent regions of Asia in the Mesozoic-Cenozoic (Triassic-lower Cretaceous)," *International Geology Review*, vol. 5, no. 1, pp. 5–27, 1963.

[43] V. S. Luchnikov, "Геология и минерально-сырьевые ресурсы Республики Таджикистан," in *Geology and mineral resources of the Republic of Tajikistan*, p. 287, Collection of scientific papers, 2001.

[44] V. I. Budanov, *Endogenous Formations of the Pamirs*, Donish, Dushanbe, 1993.

[45] R. Wolfart and H. Wittekindt, *Geologie von Afghanistan: von Reinhard Wolfart u. Hanspeter Wittekindt. Mit 76 Abb., 41 Tab. u. 3 Übersichtskt. im Text u. auf 16 Beil*, Borntraeger, Berlin, Stuttgart, 1980.

[46] E. J. Leven, "Stratigraphy of the Carboniferous-Permian volcanosedimentary sequences of the Northern Pamir, Tajikistan," *Stratigraphy and Geological Correlation*, vol. 21, no. 6, pp. 601–608, 2013.

[47] B. G. Vlasov, J. A. Dyakov, and E. S. Cherev, *Geological map of the Tajik SSR and adjacent territories*, Vsesojuznoi Geological Institute Leningrad, Saint Petersburg, 1984.

[48] S. Y. Lyoskind, L. A. Novikova, and L. G. Dolgonos, *Geological map of the USSR of 1:200000 scales: sheet J-42-XVII*, Russian Geological Research Institute, Nedra, Moscow, 1963.

[49] D. Wirtz, C. Hinze, G. Gabert, and L. Benda, *Zur geologie von Nordost-und Zentral-Afghanistan*, Geologisches Jahrbuch, 1964.

[50] F. S. Salikhov and K. S. Sakiev, "Stages of sedimentation in the Permian-Triassic North Pamirs," *Bulletin of the Institute of the National Academy of Sciences of the Kyrgyz Republic*, vol. 4, no. 2, 2014.

[51] D. Weippert, "Zur geologie des gebietes Doab-Saughan-Hajar (Nordost-Afghanistan)," in *Zur Geologie von Nordost-und Zentral-Afghanistan*, D. Wirtz, C. Hinze, G. Gabert, and L. Benda, Eds., pp. 153–183, 1964.

[52] J. Blaise, P. Bordet, J. Lang, L. A. F. De, F. Leutwein, and J. Sonet, "Mesures géochronologiques de quelques roches cristallines d'Afghanistan central," *Comptes Rendus. Académie des Sciences*, vol. 270, pp. 2772–2775, 1970.

[53] C. Montenat, "The Mesozoic of Afghanistan," *GeoArabia*, vol. 14, no. 1, pp. 147–210, 2009.

[54] A. Siehl, "Structural setting and evolution of the Afghan orogenic segment – a review," *Geological Society, London, Special Publications*, vol. 427, no. 1, pp. 57–88, 2017.

[55] M. Balini, A. Nicora, S. Zanchetta et al., "Olenekian to Early Ladinian stratigraphy of the western part of the Aghdarband window (Kopeh-Dag, NE Iran)," *Rivista Italiana di Palaeontologia e Stratigrafia*, vol. 125, pp. 283–315, 2019.

[56] A. Baud and G. M. Stämpfli, "Tectonogenesis & evolution of a segment of the Cimmerides: the volcano-sedimentary Triassic of Aghdarband (Kopet-Dagh, North-East Iran)," in *Tectonic Evolution of the Tethyan Region*, pp. 265–275, Springer, Dordrecht, 1989.

[57] H.-Q. Liu, Y.-G. Xu, Y.-T. Zhong, Z.-Y. Luo, R. M. T. R. Riley, and W. X. Le Zhang, "Crustal melting above a mantle plume: insights from the Permian Tarim Large Igneous Province, NW China," *Lithos*, vol. 326, pp. 370–383, 2019.

[58] C.-L. Zhang, Z.-X. Li, X.-H. Li, Y.-G. Xu, G. Zhou, and H.-M. Ye, "A Permian large igneous province in Tarim and Central Asian orogenic belt, NW China: results of a ca. 275 Ma mantle plume?," *Bulletin*, vol. 122, no. 11-12, pp. 2020–2040, 2010.

[59] Y.-G. Xu, X. Wei, Z.-Y. Luo, H. Q. Liu, and J. Cao, "The Early Permian Tarim Large Igneous Province: main characteristics and a plume incubation model," *Lithos*, vol. 204, pp. 20–35, 2014.

[60] D. Li, S. Yang, H. Chen et al., "Late Carboniferous crustal uplift of the Tarim plate and its constraints on the evolution of the Early Permian Tarim Large Igneous Province," *Lithos*, vol. 204, pp. 36–46, 2014.

[61] Y.-T. Zhong, Z.-Y. Luo, R. Mundil et al., "Constraining the duration of the Tarim flood basalts (northwestern China): CA-TIMS zircon U-Pb dating of tuffs," *Geological Society of America Bulletin*, vol. 134, no. 1-2, pp. 325–334, 2022.

[62] D. Konopelko, S. A. Wilde, R. Seltmann, R. L. Romer, and Y. S. Biske, "Early Permian intrusions of the Alai range: understanding tectonic settings of Hercynian post-collisional magmatism in the South Tien Shan, Kyrgyzstan," *Lithos*, vol. 302-303, pp. 405–420, 2018.

[63] F. Pirajno, J. Mao, Z. Zhang, Z. Zhang, and F. Chai, "The association of mafic-ultramafic intrusions and A-type magmatism in the Tian Shan and Altay orogens, NW China: implications for geodynamic evolution and potential for the discovery of new ore deposits," *Journal of Asian Earth Sciences*, vol. 32, no. 2-4, pp. 165–183, 2008.

[64] H. de Boorder, "Spatial and temporal distribution of the orogenic gold deposits in the Late Palaeozoic Variscides and Southern Tianshan: how orogenic are they?," *Ore Geology Reviews*, vol. 46, pp. 1–31, 2012.

[65] B. Wang, M. Faure, L. Shu et al., "Paleozoic tectonic evolution of the Yili Block, western Chinese Tianshan," *Bulletin de la Société Géologique de France*, vol. 179, no. 5, pp. 483–490, 2008.

[66] B. Wang, M. Faure, L. Shu et al., "Structural and geochronological study of high-pressure metamorphic rocks in the Kekesu section (Northwestern China): implications for the late Paleozoic tectonics of the southern Tianshan," *The Journal of Geology*, vol. 118, no. 1, pp. 59–77, 2010.

[67] J. Charvet, L. Shu, S. Laurent-Charvet et al., "Palaeozoic tectonic evolution of the Tianshan belt, NW China," *Science China Earth Sciences*, vol. 54, no. 2, pp. 166–184, 2011.

[68] K. de Jong, B. Wang, M. Faure et al., "New 40Ar/39Ar age constraints on the Late Palaeozoic tectonic evolution of the western Tianshan (Xinjiang, northwestern China), with emphasis on Permian fluid ingress," *International Journal of Earth Sciences*, vol. 98, no. 6, pp. 1239–1258, 2009.

[69] Y. Han, G. Zhao, P. A. Cawood, M. Sun, Q. Liu, and J. Yao, "Plume-modified collision orogeny: the Tarim–western Tianshan example in Central Asia," *Geology*, vol. 47, no. 10, pp. 1001–1005, 2019.

[70] R. Seltmann, D. Konopelko, G. Biske, F. Divaev, and S. Sergeev, "Hercynian post-collisional magmatism in the context of Paleozoic magmatic evolution of the Tien Shan orogenic belt," *Journal of Asian Earth Sciences*, vol. 42, no. 5, pp. 821–838, 2011.

[71] G. Hall, "Muruntau Uzbekistan: revisited," *West Australian Geologist*, vol. 465, no. 3, 2007.

[72] A. Käßner, L. Ratschbacher, J. A. Pfänder et al., "Proterozoic–Mesozoic history of the Central Asian orogenic belt in the Tajik and southwestern Kyrgyz Tian Shan: U-Pb, 40Ar/39Ar, and fission-track geochronology and geochemistry of granitoids," *GSA Bulletin*, vol. 129, no. 3-4, pp. 281–303, 2017.

[73] V. V. Vrublevskii, A. A. Morova, O. V. Bukharova, and S. I. Konovalenko, "Mineralogy and geochemistry of triassic carbonatites in the Matcha alkaline intrusive complex (Turkestan-Alai Ridge, Kyrgyz Southern Tien Shan), SW Central Asian orogenic belt," *Journal of Asian Earth Sciences*, vol. 153, pp. 252–281, 2018.

[74] V. V. Vrublevskii, "Origin of carbonatites of the Matcha alkaline pluton from Turkestan-Alai ridge, Kyrgyz Southern Tien Shan," *IOP Conference Series: Earth and Environmental Science*, vol. 110, no. 1, article 12023, 2017.

[75] J. Bershaw, C. N. Garzione, L. Schoenbohm, G. Gehrels, and L. Tao, "Cenozoic evolution of the Pamir plateau based on stratigraphy, zircon provenance, and stable isotopes of foreland basin sediments at Oytag (Wuyitake) in the Tarim Basin (West China)," *Journal of Asian Earth Sciences*, vol. 44, pp. 136–148, 2012.

[76] C. Wang, L. Liu, F. Korhonen et al., "Origins of Early Mesozoic granitoids and their enclaves from West Kunlun, NW China: implications for evolving magmatism related to closure of the Paleo-Tethys Ocean," *International Journal of Earth Sciences*, vol. 105, no. 3, pp. 941–964, 2016.

[77] R. Zhou, J. C. Aitchison, K. Lokho, E. R. Sobel, Y. Feng, and J. X. Zhao, "Unroofing the Ladakh batholith: constraints from autochthonous molasse of the Indus Basin, NW Himalaya," *Journal of the Geological Society*, vol. 177, no. 4, pp. 818–825, 2020.

[78] C. Paton, J. Hellstrom, B. Paul, J. Woodhead, and J. Hergt, "Iolite: freeware for the visualisation and processing of mass spectrometric data," *Journal of Analytical Atomic Spectrometry*, vol. 26, no. 12, pp. 2508–2518, 2011.

[79] J. Hellstrom, C. Paton, J. Woodhead, and J. Hergt, "Iolite: software for spatially resolved LA-(quad and MC) ICPMS analysis," in *Laser ablation ICP-MS in the Earth sciences: current practice and outstanding issues*, P. Sylvester, Ed., vol. 40, 2008.

[80] J. A. Petrus and B. S. Kamber, "VizualAge: a novel approach to laser ablation ICP-MS U-Pb geochronology data reduction," *Geostandards and Geoanalytical Research*, vol. 36, no. 3, pp. 247–270, 2012.

[81] M. Wiedenbeck, P. Allé, F. Corfu et al., "Three natural zircon standards for U-Th-Pb, Lu-Hf, trace element and REE analyses," *Geostandards and Geoanalytical Research*, vol. 19, no. 1, pp. 1–23, 1995.

[82] L. P. Black, S. L. Kamo, C. M. Allen et al., "Improved $^{206}Pb/^{238}U$ microprobe geochronology by the monitoring of a trace-element-related matrix effect; SHRIMP, ID-TIMS, ELA-ICP-MS and oxygen isotope documentation for a series of zircon standards," *Chemical Geology*, vol. 205, no. 1-2, pp. 115–140, 2004.

[83] S. E. Jackson, N. J. Pearson, W. L. Griffin, and E. A. Belousova, "The application of laser ablation-inductively coupled plasma-mass spectrometry to in situ U-Pb zircon geochronology," *Chemical Geology*, vol. 211, no. 1-2, pp. 47–69, 2004.

[84] X. Liu, S. Gao, C. Diwu, H. L. Yuan, and Z. C. Hu, "Simultaneous in-situ determination of U-Pb age and trace elements

in zircon by LA-ICP-MS in 20 μm spot size," *Chinese Science Bulletin*, vol. 52, no. 9, pp. 1257–1264, 2007.

[85] U. Schaltegger, M. Ovtcharova, S. P. Gaynor et al., "Long-term repeatability and interlaboratory reproducibility of high-precision ID-TIMS U-Pb geochronology," *Journal of Analytical Atomic Spectrometry*, vol. 36, no. 7, pp. 1466–1477, 2021.

[86] I. Dunkl, T. Mikes, D. Frei, A. Gerdes, R. Tolosana-Delgado, and H. V. Eynatten, "UranOS: data reduction program for time-resolved U/Pb analyses," http://www.sediment.uni-goettingen.de/staff/dunkl/software/uranos.html.

[87] A. Bande, E. R. Sobel, A. Mikolaichuk, A. Schmidt, and D. F. Stockli, "Exhumation history of the western Kyrgyz Tien Shan: implications for intramontane basin formation," *Tectonics*, vol. 36, no. 1, pp. 163–180, 2017.

[88] M. S. A. Horstwood, J. Košler, G. Gehrels et al., "Community-derived standards for LA-ICP-MS U-(Th-)Pb geochronology – uncertainty propagation, age interpretation and data reporting," *Geostandards and Geoanalytical Research*, vol. 40, no. 3, pp. 311–332, 2016.

[89] R Development Core Team, *R: a language and environment for statistical computing, 2011*, R Foundation for Statistical Computing, Vienna, Austria, 2019, https://www.R-project.org.

[90] P. Vermeesch, "IsoplotR: a free and open toolbox for geochronology," *Geoscience Frontiers*, vol. 9, no. 5, pp. 1479–1493, 2018.

[91] P. Vermeesch, "Unifying the U–Pb and Th–Pb methods: joint isochron regression and common Pb correction," *Geochronology*, vol. 2, no. 1, pp. 119–131, 2020.

[92] E. Zuleger and J. Erzinger, "Determination of the REE and Y in silicate materials with ICP-AES," *Fresenius' Zeitschrift für Analytische Chemie*, vol. 332, no. 2, pp. 140–143, 1988.

[93] W. Pretorius, D. Weis, G. Williams, D. Hanano, B. Kieffer, and J. Scoates, "Complete trace elemental characterisation of granitoid (USGS G-2, GSP-2) reference materials by high resolution inductively coupled plasma-mass spectrometry," *Geostandards and Geoanalytical Research*, vol. 30, no. 1, pp. 39–54, 2006.

[94] R. L. Romer and K. Hahne, "Life of the Rheic Ocean: scrolling through the shale record," *Gondwana Research*, vol. 17, no. 2-3, pp. 236–253, 2010.

[95] P. Dulski, "Reference materials for geochemical studies: new analytical data by ICP-MS and critical discussion of reference values," *Geostandards Newsletter*, vol. 25, no. 1, pp. 87–125, 2001.

[96] V. Janoušek, C. M. Farrow, and V. Erban, "Interpretation of whole-rock geochemical data in igneous geochemistry: introducing GeoChemical Data ToolKit (GCDkit)," *Journal of Petrology*, vol. 47, no. 6, pp. 1255–1259, 2006.

[97] P. Vermeesch, "On the treatment of discordant detrital zircon U–Pb data," *Geochronology*, vol. 3, no. 1, pp. 247–257, 2020.

[98] C. J. Spencer, C. L. Kirkland, and R. J. M. Taylor, "Strategies towards statistically robust interpretations of in situ U-Pb zircon geochronology," *Geoscience Frontiers*, vol. 7, no. 4, pp. 581–589, 2016.

[99] S.-S. Sun and W. F. McDonough, "Chemical and isotopic systematics of oceanic basalts: implications for mantle composition and processes," *Geological Society, London, Special Publications*, vol. 42, no. 1, pp. 313–345, 1989.

[100] W. V. Boynton, "Chapter 3 - Cosmochemistry of the rare earth elements: meteorite studies," *Developments in Geochemistry*, vol. 2, pp. 63–114, 1984.

[101] T. Ohta and H. Arai, "Statistical empirical index of chemical weathering in igneous rocks: a new tool for evaluating the degree of weathering," *Chemical Geology*, vol. 240, no. 3-4, pp. 280–297, 2007.

[102] M. J. Le Bas, R. W. Le Maitre, A. Streckeisen, and B. Zanettin, "A chemical classification of volcanic rocks based on the total alkali-silica diagram," *Journal of Petrology*, vol. 27, no. 3, pp. 745–750, 1986.

[103] A. Peccerillo and S. R. Taylor, "Geochemistry of Eocene calc-alkaline volcanic rocks from the Kastamonu area, northern Turkey," *Contributions to Mineralogy and Petrology*, vol. 58, no. 1, pp. 63–81, 1976.

[104] B. R. Frost, C. G. Barnes, W. J. Collins, R. J. Arculus, D. J. Ellis, and C. D. Frost, "A geochemical classification for granitic rocks," *Journal of Petrology*, vol. 42, no. 11, pp. 2033–2048, 2001.

[105] T. E. Cerling, F. H. Brown, and J. R. Bowman, "Low-temperature alteration of volcanic glass: hydration, Na, K, ^{18}O and Ar mobility," *Chemical Geology: Isotope Geoscience section*, vol. 52, no. 3-4, pp. 281–293, 1985.

[106] H. Staudigel, S. R. Hart, and S. H. Richardson, "Alteration of the oceanic crust: processes and timing," *Reports of the Deep Sea Drilling Project*, vol. 9, pp. 10–12, 1981.

[107] A. J. Spivack and H. Staudigel, "Low-temperature alteration of the upper oceanic crust and the alkalinity budget of seawater," *Chemical Geology*, vol. 115, no. 3-4, pp. 239–247, 1994.

[108] J. W. Shervais, "Ti-V plots and the petrogenesis of modern and ophiolitic lavas," *Earth and Planetary Science Letters*, vol. 59, no. 1, pp. 101–118, 1982.

[109] J. A. Pearce, "Trace element characteristics of lavas from destructive plate boundaries," in *Orogenic andesites and related rocks*, R. S. Thorpe, Ed., pp. 528–548, John Wiley and Sons, Chichester, England, 1982.

[110] E. D. Mullen, "$MnO/TiO_2/P_2O_5$: a minor element discriminant for basaltic rocks of oceanic environments and its implications for petrogenesis," *Earth and Planetary Science Letters*, vol. 62, no. 1, pp. 53–62, 1983.

[111] J. C. Bailey, "Geochemical Criteria for a Refined Tectonic Discrimination of Orogenic Andesites," *Chemical Geology*, vol. 32, no. 1-4, pp. 139–154, 1981.

[112] J. Morin, M. Jolivet, D. Shaw, S. Bourquin, and E. Bataleva, "New sedimentological and palynological data from the Yarkand-Fergana Basin (Kyrgyz Tian Shan): insights on its Mesozoic paleogeographic and tectonic evolution," *Geoscience Frontiers*, vol. 12, no. 1, pp. 183–202, 2021.

[113] J. Liu, H. Wang, L. I. Shehong, T. Laixi, and R. Guangli, "Geological and geochemical features and geochronology of the Kayizi porphyry molybdenum deposit in the northern belt of western Kunlun, NW China," *Acta Petrologica Sinica*, vol. 26, no. 10, pp. 3095–3105, 2010.

[114] S. Lallemand, A. Heuret, and D. Boutelier, "On the relationships between slab dip, back-arc stress, upper plate absolute motion, and crustal nature in subduction zones," *Geochemistry, Geophysics, Geosystems*, vol. 6, no. 9, 2005.

[115] M. Mamani, G. Wörner, and T. Sempere, "Geochemical variations in igneous rocks of the central Andean orocline (13 S to 18 S): tracing crustal thickening and magma generation through time and space," *Bulletin*, vol. 122, no. 1-2, pp. 162–182, 2010.

[116] S.-K. Kufner, B. Schurr, C. Sippl et al., "Deep India meets deep Asia: lithospheric indentation, delamination and

break-off under Pamir and Hindu Kush (Central Asia)," *Earth and Planetary Science Letters*, vol. 435, pp. 171–184, 2016.

[117] D. Rutte, L. Ratschbacher, S. Schneider et al., "Building the Pamir-Tibetan plateau—crustal stacking, extensional collapse, and lateral extrusion in the central Pamir: 1. Geometry and kinematics," *Tectonics*, vol. 36, no. 3, pp. 342–384, 2017.

[118] B. Taylor and F. Martinez, "Back-arc basin basalt systematics," *Earth and Planetary Science Letters*, vol. 210, no. 3-4, pp. 481–497, 2003.

[119] F. Martinez, K. Okino, Y. Ohara, A. L. Reysenbach, and S. Goffredi, "Back-arc basins," *Oceanography*, vol. 20, no. 1, pp. 116–127, 2007.

[120] A. Bézos, S. Escrig, C. H. Langmuir, P. J. Michael, and P. D. Asimow, "Origins of chemical diversity of back-arc basin basalts: a segment-scale study of the eastern Lau spreading center," *Journal of Geophysical Research*, vol. 114, no. B6, p. B6, 2009.

[121] A. Zanchi, S. Zanchetta, M. Balini, and M. R. Ghassemi, "Oblique convergence during the Cimmerian collision: evidence from the Triassic Aghdarband Basin, NE Iran," *Gondwana Research*, vol. 38, pp. 149–170, 2016.

[122] S. Zanchetta, F. Berra, A. Zanchi et al., "The record of the Late Palaeozoic active margin of the Palaeotethys in NE Iran: constraints on the Cimmerian orogeny," *Gondwana Research*, vol. 24, no. 3-4, pp. 1237–1266, 2013.

[123] V. S. Burtman, "Cenozoic crustal shortening between the Pamir and Tien Shan and a reconstruction of the Pamir-Tien Shan transition zone for the Cretaceous and Palaeogene," *Tectonophysics*, vol. 319, no. 2, pp. 69–92, 2000.

[124] E. R. Sobel and T. A. Dumitru, "Thrusting and exhumation around the margins of the western Tarim basin during the India-Asia collision," *Journal of Geophysical Research: Earth Surface*, vol. 102, no. B3, pp. 5043–5063, 1997.

[125] K. Teshebaeva, H. Sudhaus, H. Echtler, B. Schurr, and S. Roessner, "Strain partitioning at the eastern Pamir-Alai revealed through SAR data analysis of the 2008 Nura earthquake," *Geophysical Journal International*, vol. 198, no. 2, pp. 760–774, 2014.

[126] T. Li, Z. Chen, J. Chen et al., "Along-strike and downdip segmentation of the Pamir frontal thrust and its association with the 1985 Mw 6.9 Wuqia earthquake," *Journal of Geophysical Research: Solid Earth*, vol. 124, no. 9, pp. 9890–9919, 2019.

[127] M. Patyniak, A. Landgraf, A. Dzhumabaeva et al., "The Pamir frontal thrust fault: Holocene full-segment ruptures and implications for complex segment interactions in a continental collision zone," *Journal of Geophysical Research: Solid Earth*, vol. 126, no. 12, 2021.

[128] X. Qiao, Q. Wang, S. Yang, J. Li, R. Zou, and K. Ding, "The 2008 Nura Mw6.7 earthquake: a shallow rupture on the Main Pamir Thrust revealed by GPS and InSAR," *Geodesy and Geodynamics*, vol. 6, no. 2, pp. 91–100, 2015.

[129] K. Cohen, D. A. Harper, and P. Gibbard, *International chronostratigraphic chart (v 2020/03)*, International Commission on Stratigraphy. Hentet fra, 2020, https://stratigraphy.org/icschart/ChronostratChart2020-03.pdf.

[130] J. Siivola and R. Schmid, *List of mineral abbreviations*, Cambridge University Press, New York, 2007.